PARP14 is an interferon (IFN)-induced host factor that promotes IFN production and affects the replication of multiple viruses

Srivatsan Parthasarathy[1], Pradtahna Saenjamsai[1], Hongping Hao[1], Anna Ferkul[1], Jessica J. Pfannenstiel[1], Daniel S. Bejan[2], Yating Chen[3], Ellen L. Suder[4,5,6], Nancy Schwarting[1], Masanori Aikawa[7,8,9], Elke Muhlberger[4,5,6], Adam J. Hume[4,5,6], Robin C. Orozco[1], Christopher S. Sullivan[3], Michael, S. Cohen[2], David J. Davido[1], Anthony R. Fehr[1*]

[1]Department of Molecular Biosciences, University of Kansas, Lawrence, Kansas 66045, USA
[2]Department of Chemical Physiology and Biochemistry, Oregon Health Sciences University, Portland, OR, 97239, USA
[3]Department of Molecular Biosciences, University of Texas, Austin, TX, 78712, USA
[4]Department of Microbiology, Boston University School of Medicine, Boston, MA, 02118, USA
[5]National Emerging Infectious Diseases Laboratories, Boston University, Boston, MA, 02118, USA
[6]Center for Emerging Infectious Diseases Policy & Research, Boston University, Boston, MA, 02118, USA
[7]Center for Excellence in Vascular Biology (P.K.J., M.A., E.A.), Brigham and Women's Hospital, Harvard Medical School, Boston, MA, 02115, USA.
[8]Center for Interdisciplinary Cardiovascular Sciences (M.A., E.A.), Brigham and Women's Hospital, Harvard Medical School, Boston, MA, 02115, USA.
[9]Channing Division of Network Medicine (M.A.), Brigham and Women's Hospital, Harvard Medical School, Boston, MA, 02115, USA.

*Corresponding author: Dr. Anthony R. Fehr, Molecular Biosciences, University of Kansas, Lawrence, Kansas, USA, Tele: 785-864-6626

Email : arfehr@ku.edu

Running title : PARP14 promotes IFN and affects the replication of multiple viruses

Keywords: ADP-ribosylation, PARP, macrodomain, coronavirus, HSV-1, Ebola virus, Nipah virus, VSV, LCMV, interferon, interferon-stimulated genes

ABSTRACT

PARP14 is a 203 kDa multi-domain protein that is primarily known as an ADP-ribosyltransferase, and is involved in a variety of cellular functions including DNA damage, microglial activation, inflammation, and cancer progression. In addition, PARP14 is upregulated by interferon (IFN), indicating a role in the antiviral response. Furthermore, PARP14 has evolved under positive selection, again indicating that it is involved in host-pathogen conflict. We found that PARP14 is required for increased IFN-I production in response to coronavirus infection lacking ADP-ribosylhydrolase (ARH) activity and poly(I:C), however, whether it has direct antiviral function remains unclear. Here we demonstrate that the catalytic activity of PARP14 enhances IFN-β and IFN-λ responses and restricts ARH-deficient murine hepatitis virus (MHV) and severe acute respiratory syndrome coronavirus 2 (SARS-CoV-2) replication. To determine if PARP14's antiviral functions extended beyond CoVs, we tested the ability of herpes simplex virus 1 (HSV-1), a DNA virus, vesicular stomatitis virus (VSV), a negative-sense RNA virus, and lymphocytic choriomeningitis virus (LCMV), an ambisense RNA virus, to infect A549 PARP14 knockout (KO) cells. While LCMV infection was unaffected, HSV-1 replication was increased in PARP14 KO cells and VSV replication was decreased. These results indicate that PARP14 restricts HSV-1 replication but enhances the replication of VSV. A PARP14 active site inhibitor had no impact on HSV-1 or VSV replication, indicating that its effect on these viruses was independent of its catalytic activity. These data demonstrate that PARP14 promotes IFN production and has both proviral and antiviral functions targeting multiple viruses.

54 **IMPORTANCE**

55 The antiviral response is largely regulated by post-translation modifications (PTM), including
56 ADP-ribosylation. PARP14 is an ADP-ribosyltransferase that is upregulated by interferon and is
57 under positive selection, indicating that it is involved in host-pathogen conflict. However, no anti-
58 viral function has been described for PARP14. Here, we found that PARP14 represses both
59 coronavirus and HSV-1 replication, demonstrating that PARP14 has antiviral functions.
60 Surprisingly, we also found that PARP14 also has pro-viral functions, as it was critical for the
61 efficient replication of VSV. These data indicate that PARP14 has both proviral and antiviral
62 functions. Defining the mechanisms used by PARP14 to both repress and promote virus replication
63 will provide new insights into how PARPs regulate virus infection.

64 **INTRODUCTION**

65 Virus infection causes activation of host immune responses, with the interferon (IFN) response
66 being the major pathway activated. Recognition of viral pathogen-associated molecular patterns
67 (PAMPs) by host surface and cytosolic receptors leads to a series of molecular events that activates
68 the expression of different types of IFNs, that eventually upregulates the expression of anti-viral
69 IFN stimulated genes (ISGs). Several different post-translational modifications regulate this
70 response, including phosphorylation, ubiquitination, and other less common modification such as
71 ADP-ribosylation.

72 ADP-ribosylation is a post-translational modification (PTM) where ADP-ribose subunits are
73 added to target proteins in a process catalyzed by ADP-ribosyltransferases (ARTs) that use NAD^+
74 as a substrate. The ART Diphtheria toxin-like domain (ARTD) family of ART proteins are
75 intracellular ARTs that are individually named PARPs [1]. These ARTDs catalyze the addition of
76 either poly-ADP-ribose (PAR) or mono-ADP-ribose (MAR) to proteins or nucleic acid. The
77 human genome encodes 17 PARPs that are involved in the regulation of most cellular activities
78 including DNA damage repair, ER stress, cell cycle regulation, transcription and translation, and
79 the innate and adaptive immune responses [1]. Apart from addition of ADP-ribose, removal of
80 ADP-ribose from target proteins is also implicated in important cellular processes. The presence
81 of ADP-ribose hydrolases (ARH) or macrodomains such as PARG, TARG1, MacroD1 and
82 MacroD2 in humans underscores the importance of ADP-ribose turnover [2]. Furthermore, all
83 coronaviruses (CoVs) encode for a highly conserved macrodomain (Mac1) that removes ADP-
84 ribose from proteins, indicating that these viruses may be susceptible to antiviral ADP-
85 ribosylation. Infection with murine hepatitis virus (MHV), SARS-CoV, or SARS-CoV-2
86 containing point mutants in key residues required for catalytic activity (i.e. MHV N1347A) or full

87 deletions of Mac1 induce robust interferon responses and are highly attenuated *in vivo* [3-5]. In
88 addition, the poor replication and enhanced induction of IFN following infection with MHV N1347A could
89 be reversed using PARP inhibitiors [3]. These results demonstrated that PARP-mediated ADP-ribosylation
90 is a potent anti-viral defense mechanism against CoVs.

91 The expression of several PARPs is activated by IFN in response to virus infection, categorizing
92 them as interferon stimulated genes (ISGs). Some PARPs have known antiviral activity including
93 PARP13 (zinc-antiviral protein or ZAP), PARP12, PARP11, PARP9, PARP5a/b, PARP7, and
94 PARP1 [6]. In addition, some PARPs also act as pro-viral factors, promoting viral replication and
95 infection. PARP11 was shown to suppress IFN-I signaling by MARylating IFNAR and priming it
96 for ubiquitination and eventual degradation. The suppression of IFN-I signaling by PARP11
97 increased the replication of vesicular stomatitis virus (VSV) and herpes simplex virus 1 (HSV-1).
98 These results demonstrated a pro-viral role for PARP11 [7]. PARP7-dependent ADP-ribosylation
99 also suppressed IFN-I production and promoted influenza A virus infection, indicating that PARP7
100 also has pro-viral functions [8]. Consistent with this pro-viral function, PARP7 knockdown
101 reduced the replication of murine hepatitis virus (MHV) A59, demonstrating its ability to promote
102 coronavirus replication [3]. Finally, PARP1 inhibitors have also been shown to efficiently inhibit
103 replication of several viruses such as herpesviruses, adenoviruses and human immunodeficiency
104 virus (HIV), indicating that PARP1 may also promote virus replication in some cases [9-11].

105 PARP14 is an ISG that is important in several different biological processes including
106 inflammation, cancer progression and DNA damage. PARP14 is a multidomain protein and its
107 domain architecture was recently re-analyzed using Alphafold2 [12]. This analysis determined that
108 PARP14 contains 3 RRM domains, 7 full KH domains and 1 split KH domain that are suspected
109 to bind to nucleic acids, 3 macrodomains (MDs) one of which has an ADP-ribose hydrolase

110 activity (MD1) [12-14], a WWE domain that is suspected to bind ADP-ribose subunits, and the
111 ART catalytic domain [12].

112 PARP14 was originally identified as a STAT6-binding protein that promoted IL-4 dependent anti-
113 inflammatory signaling [15]. Since then, several independent studies have implicated PARP14 in
114 inflammatory and interferon signaling pathways. PARP14's involvement in inflammatory and IFN
115 responses is cell-type and insult dependent, suggesting that PARP14 has multiple functions that
116 are context dependent. In M1 macrophages PARP14 suppresses IFNγ-induced activation of pro-
117 inflammatory signaling by STAT1 MARylation [16]. We and others have found that PARP14 is
118 also critical for inducing high levels of IFN-β following infection with *Salmonella typhimurium*,
119 MHV, as well as treatments with LPS or poly(I:C) treatment [3, 17]. Specifically, PARP14
120 knockout M0 macrophages and epithelial cells demonstrated significantly reduced levels of IFN-
121 β after infection or treatment with LPS or poly(I:C), indicating that one of PARP14's functions is
122 to promote IFN-β production, however the mechanisms by which it enhances IFN-β production
123 remain unknown [3, 17]. More recently, several groups have demonstrated that PARP14 is the
124 major PARP responsible for IFN-γ and poly(I:C) induced cytosolic ADP-ribose bodies (ICAB)
125 [18-21].

126 Interestingly, PARP14 is one of the several PARPs that has evolved under positive selection,
127 indicating that it may be involved in host-pathogen conflicts. This positive selection is seen in
128 many of the different domains of PARP14, especially the macrodomains, WWE domain, and the
129 catalytic domain at the C-terminus of the protein [22]. However, despite this evidence for
130 involvement in host-pathogen interactions, there are very few reports describing any impact of
131 PARP14 on virus or bacterial infections. In one report, PARP14 KO RAW264.7 macrophages had
132 significantly increased levels of *S. typhimurium* replication [17]. In addition, siRNA knockdown

133 of PARP14 led to a mild increase (~2-fold) in the levels of a Mac1 mutant MHV viral RNA, but
134 knockdown or a congenital knockout of PARP14 did not significantly increase the amount of
135 infectious virus produced [3]. Despite PARP14 being a regulator of IFN production and triggers
136 the production of ICABs, it remains unclear how or even if PARP14 impacts virus replication.

137 Recently, several tools have been developed to facilitate testing the impact of PARP14 on virus
138 infection. First, we reported PARP14 knockout (KO) A549 and NHDF cell lines [3], which have
139 intact IFN systems and are susceptible to infection by a wide variety of viruses. Second, a highly
140 potent and selective PARP14 catalytic inhibitor, RBN01239, was developed [23]. Finally, we
141 report here the creation of a tamoxifen-inducible PARP14 knockout mouse model. Hence, with
142 the availability of an advanced PARP14 inhibitor and with the advent of several PARP14 knock-
143 out systems, we sought to determine the effect of PARP14 and its catalytic activity on IFN
144 production and the replication of multiple different virus families.

145 Utilizing these tools, we report here that PARP14 influences the replication of multiple viruses.
146 PARP14 potently inhibited the replication of HSV-1 as well as Mac1-mutant MHV and SARS-
147 CoV-2. Unexpectedly, PARP14 also acted as a proviral factor for vesicular stomatitis virus (VSV),
148 a negative-sense RNA virus, highlighting the multifaceted effect of PARP14 on virus replication.
149 Furthermore, we confirmed that the catalytic activity of PARP14 was critical for IFN-β and IFN-
150 λ induction and the inhibition of CoV replication. This study highlights the involvement of
151 PARP14 in the IFN response and virus infection, underscoring the importance of PARP14 as an
152 immunomodulatory host factor that can affect the replication of multiple viruses.

153 **RESULTS**

154 **PARP14 promotes IFN-β and IFN-λ production in poly(I:C) transfected cells.**

155 We previously demonstrated that PARP14 was required for IFN-β production in response
156 to poly(I:C) in human A549 cells, via an indirect VSV bioassay [3]. To determine how PARP14
157 impacts IFN induction more quantitatively, we induced IFN production via poly(I:C) transfection
158 and quantified the amount of IFN-β and IFN-λ transcripts by qPCR and protein by ELISA in A549
159 wild-type (WT) and PARP14 KO cells, that were developed using CRISPR by transducing A549
160 cells with control or PARP14 targeting guide RNAs and Cas9 [3]. Poly(I:C) transfection induced
161 IFN-β **(Fig. 1A, S1A)** and IFN-λ **(Fig. 1B)** mRNA production in A549 cells, but their levels were
162 significantly reduced in PARP14 KO compared to WT A549 cells. We also observed a similar
163 decrease in IFN-β and IFN-λ protein levels following poly(I:C) transfection in PARP14 KO A549
164 cells compared to WT cells in an ELISA assay **(Fig. 1C-D)**. Poly(I:C) transfected PARP14 KO
165 cells also had decreased protein levels of the interferon stimulated gene OAS3 compared to WT
166 cells **(Fig. 1E-F)**. Finally, we also observed a nearly 4-fold reduction in IFN-β mRNA production
167 in response to poly(I:C) transfection in PARP14 KO NHDF cells **(Fig. S1B)** [3]. Since PARP14
168 catalyzes MARylation, we used a highly potent and selective PARP14 catalytic inhibitor,
169 RBN012759 (PARP14i) to test if the observed reduction in IFN and ISG levels were due to the
170 MARylating activity of PARP14. PARP14i efficiently restricted PARP14's auto-MARylation
171 activity in PARP14 overexpressing 293T cells in a dose-dependent manner **(Fig. S1B)**. We utilized
172 PARP14 G832E for these experiments as it was shown to be deficient in its MD1-dependent ADP-
173 ribosyl hydrolase activity, which leads to enhanced autoMARylation [14]. Importantly, poly(I:C)
174 stimulated A549 cells displayed a dose-dependent decrease in IFN-β transcript levels when treated
175 with PARP14i. At the highest concentration of PARP14i, the level of IFN-β mirrored those in
176 PARP14 KO cells **(Fig. 1G)**. This suggests that the reduction in IFN-β levels in PARP14 KO cells
177 was due to the absence of PARP14 catalytic activity. In addition, we also used a PARP14

178 degrading compound, RBN012811 (DEG), and its associated negative control, RBN013527
179 (CTL), to test the role of PARP14 in IFN-β production (a generous gift from Mario Niepel, Ribon
180 Therapeutics) [24]. DEG effectively reduced PARP14 protein to undetectable levels in WT A549
181 cells **(Fig. S1C)**. Compared to CTL, we found that the PARP14 DEG decreased IFN-β mRNA
182 induction 3-fold, similar to results with complete PARP14 KO cells **(Fig. S1D)**. Finally, we
183 restored IFN-β transcript and protein abundance to near WT levels by exogenously expressing full-
184 length PARP14 in PARP14 KO cells **(Fig. 1H-I)**, further confirming that the decrease in IFN-β
185 levels in PARP14 KO cells was not due to off-target effects of the PARP14 deletion. These results
186 demonstrate that in response to poly(I:C) stimulation PARP14-dependent MARylation promotes
187 IFN-β and IFN-λ production.

188 **PARP14 promotes IFN-β production in Mac1-mutant CoV infected cells.**

189 Using congenital PARP14 KO mouse cells, we previously showed that PARP14 was required to
190 promote IFN-β production upon infection with MHV- N1347A [3]. To circumvent the limitations
191 of constitutive PARP14 KO mice, which include poor breeding efficiency and potential
192 confounding effects of developmental compensation for PARP14 KO by other PARPs, we
193 developed a conditional tamoxifen-inducible PARP14 KO mouse model to better identify the role
194 of PARP14 in response to MHV infection **(Fig. 2A)**. *LoxP* sites were inserted into the *parp14*
195 locus around exon 2 via CRISPR mediated mutagenesis to create *parp14* floxed alleles. These
196 mice were then bred with *ert2-cre* heterozygote mice to obtain both *parp14* floxed *ert2-cre*
197 positive mice (*parp14*$^{flox/Ert2\text{-}Cre}$), and as controls, *parp14* floxed ert2-*cre* negative offspring
198 (*parp14*$^{+/+}$) **(Fig. 2A)**. BMDMs were harvested from these mice and in *cre* positive cells induction
199 with 4-hydroxy tamoxifen (4-OH-T) led to an efficient knock-out of PARP14 *(Parp14*$^{-/-}$*)* **(Fig**
200 **S2A)**. BMDMs that were *cre* negative still expressed PARP14 following treatment with 4-OH-T

201 (*parp14*$^{+/+}$). MHV-N1347A infection induced robust IFN-β levels compared to WT in *parp14*$^{+/+}$
202 BMDMs as previously demonstrated **(Fig. 2B)** [3]. However, in *parp14*$^{-/-}$ BMDMs infected with
203 N1347A, the level of IFN-β was reduced to *parp14*$^{+/+}$ BMDM levels infected with WT virus,
204 suggesting that PARP14 was required for IFN-β production in response to MHV-N1347A
205 infection, confirming our prior observation and validating our KO mice **(Fig 2B)**. Similarly, there
206 was also a decrease in the induction of ISG15 transcript levels in MHV-N1347A infected cells in
207 *parp14*$^{-/-}$ cells **(Fig S2B)**. To determine if PARP14's ART activity was responsible for the increase
208 in IFN-*β* expression following infection, MHV-WT and N1347A infected BMDMs were treated
209 with PARP14i and tested for IFN-β mRNA expression. PARP14i treatment caused a dose-
210 dependent decrease in IFN-β expression in BMDMs infected with N1347A **(Fig. 2D)** similar to its
211 impact on poly(I:C) induced IFNβ expression. Following MHV-N1347A infection, the level of
212 secreted IFN-β protein was also reduced to WT levels in *Parp14*$^{-/-}$ BMDMs and in WT BMDMs
213 treated with PARP14i **(Fig. 2E)**. Previously, we demonstrated that infection with a Mac1 deleted
214 SARS-CoV-2 virus (ΔMac1) induced elevated levels of IFN-*β* and IFN-*λ* in human epithelial
215 cells, which we hypothesized was due to PARP14 as it was highly upregulated following infection,
216 though this was not formally proven [25]. Following ΔMac1 infection of Calu-3 cells, PARP14i
217 treatment of Calu-3 cells reduced the mRNA levels of IFN-β, IFN-λ and CXCL-10 to levels seen
218 following WT virus infection **(Fig. 2F)**. These data demonstrate that the increase in IFN-β levels
219 in response to Mac1-deficient human and mouse CoV infection occurs via PARP14-dependent
220 MARylation.

221 **PARP14 promotes MDA-5 but not RIG-I dependent IFN production.**

222 IFN stimulation in virus-infected cells occurs due to recognition of viral RNA by pattern
223 recognition receptors such as MDA5 or RIG-I. This leads to a cascade of events, resulting in

224 activation of cytoplasmic proteins such as MAVS, TBK-1 and IRF3 and the nuclear translocation
225 of IRF3 that leads to transcriptional activation of IFN production. BMDMs infected with N1347A
226 MHV-JHM induced a robust production of IFN-β compared to WT infection. However, this
227 difference in IFN-β production was lost during N1347A infection in BMDMs from MAVS knock-
228 out (KO) (MAVS$^{-/-}$) mice demonstrating the key role of intracellular RNA sensing for the
229 induction of IFN-β **(Fig. 3A)**. We then tested the effect of MDA5 and RIG-I KO (Mda5$^{-/-}$ and RIG-
230 I$^{-/-}$) on IFN-β production following infection with N1347A **(Fig. 3A)**. We found that RIG-I KO
231 did not have any effect on IFN-β production during N1347A infection. In contrast, IFN-β levels
232 were reduced to WT levels in Mda5$^{-/-}$ BMDMs, suggesting the IFN-β production during N1347A
233 infection occurred via the MDA5-dependent IFN-production pathway. Next, we tested to whether
234 PARP14 specifically regulated MDA5-dependent IFN-β production by overexpressing MDA5 or
235 RIG-I in A549 cells, which is known to induce IFN expression. IFN-β production due to exogenous
236 expression of RIG-I remained unaffected following PARP14i treatment. However, there was a
237 significant ~3-fold reduction in IFN-β production following PARP14i treatment in MDA5
238 expressing cells **(Fig. 3B)**. To corroborate these findings we use two different viruses, Sendai virus
239 (SeV) and encephalomyocarditis virus (EMCV), that are specific agonists of RIG-I and MDA5,
240 respectively. PARP14i treatment reduced IFN-β production ~3-fold during EMCV infection but
241 had no effect on SeV induced IFN production in BMDMs **(Fig. 3C)** and A549 cells **(Fig. 3D)**.
242 These results indicate that PARP14 promotes MDA5 but not RIG-I dependent IFN-β production.

243 **RNAseq analysis identifies over 100 genes up-regulated by PARP14.**

244 Next, we used RNAseq to identify all genes that are influenced by PARP14-dependent
245 MARylation, in addition to IFNs and ISGs. To identify PARP14 regulated genes, we analyzed the
246 transcriptome of BMDMs that are infected by N1347A with and without PARP14i. As expected

247 from previous studies, N1347A infected DMSO-treated BMDMs had elevated levels of IFN-I,
248 ISGs, and dozens of other genes involved in antiviral immunity. Upon treatment with PARP14i,
249 the mRNA levels of a substantial number of these genes were reduced, indicating that these
250 mRNAs are increased by PARP14-dependent MARylation. Overall, we found that 622 genes were
251 upregulated by PARP14, while 355 genes were downregulated, for a total number of 977
252 differentially expressed genes expressed above a threshold fold change (FC) of 1.5-fold and
253 threshold P-adjusted value of 0.001 **(Fig. 4A)**. Next, we performed a functional analysis on the
254 genes that are regulated by PARP14 MARylation activity. Many of the genes promoted by
255 PARP14 were genes involved in antiviral immunity **(Fig 4B)**. However, genes involved in
256 apoptosis, transcription, and ubiquitin ligase conjugation were also upregulated. Representative
257 genes from each of these pathways were validated by qPCR **(Fig. 4C)**. Furthermore, we took a
258 closer look at some of the genes observed to be upregulated or downregulated over 20-fold. These
259 genes were found to cluster in biological processes of transcription and transcriptional regulation
260 with very low p-value (upon functional enrichment analysis by DAVID). Overall, this data
261 suggests that PARP14 is an important regulator of antiviral immunity but may also regulate other
262 cellular processes such as cell death and transcription.

263 **PARP14 is required for the repression of Mac1-mutant coronavirus replication.**

264 We previously found that *parp14* knockdown mildly increased the replication of MHV-
265 N1347A in BMDMs, however congenital *parp14* KO mice did not have increased MHV-N1347A
266 replication [3]. To determine if PARP14 was required to repress MHV-N1347A, we infected our
267 *parp14*$^{-/-}$ and *parp14*$^{+/+}$ BMDMs as described above. As previously observed, MHV-N1347A had
268 a significant growth defect compared to MHV-WT virus in *parp14*+/+ cells, regardless of whether
269 the cells were or were not treated with tamoxifen **(Fig. 5A)**. Interestingly, *parp14*$^{-/-}$ mostly restored

270 the replication of MHV-N1347A, suggesting that PARP14 is required for restricting MHV-
271 N1347A virus replication in BMDMs **(Fig. 5B)**. We also found that MHV-N1347A replication
272 was increased to levels similar to those of MHV-WT in *parp14*$^{-/-}$ bone-marrow-derived dendritic
273 cells (BMDCs) **(Fig. 5C)**. To test whether this increased MHV-N1347A replication in *parp14*$^{-/-}$
274 cells is due to PARP14-dependent MARylation, we measured MHV-N1347A replication in the
275 presence and absence of PARP14i. In the presence of PARP14i, N1347A replication was similarly
276 restored to near WT levels, suggesting that the catalytic activity of PARP14 was required for
277 restricting MHV-N1347A replication **(Fig. 5D)**.

278 We next tested whether PARP14 was required to restrict the replication of severe acute
279 respiratory syndrome coronavirus 2 (SARS-CoV-2) ΔMac1. We previously found that SARS-
280 CoV-2 ΔMac1 replicates near SARS-CoV-2 levels in Calu-3 cells, but that SARS-CoV-2ΔMac1
281 is more sensitive to IFN-γ pre-treatment than WT virus, and IFN-γ induces the expression of
282 several PARPs, including PARP14 [25]. To determine if PARP14 is required for IFN-γ mediated
283 restriction of SARS-CoV-2ΔMac1, we infected IFN-γ pretreated Calu3 cells with SARS-CoV-2
284 WT and ΔMac1 with and without PARP14i. Upon treatment with PARP14i, we observed that WT
285 virus was not impacted either in the presence or absence of IFN-γ, in contrast, the replication of
286 SARS-CoV-2ΔMac1 in cells pre-treated with IFN-γ was significantly increased to levels near that
287 of non-IFN-γ treated cells **(Fig. 5E)**. Overall, these results suggest that MARylation triggered by
288 PARP14 is required to restrict the replication of Mac1-deficient MHV and SARS-CoV-2 viruses.

289 **PARP14 restricts HSV-1 replication.**

290 PARP14 is one of several PARPs that has evolved under positive selection in primates,
291 indicating that it is involved in host-pathogen conflict [22]. Thus, we hypothesized that in addition
292 to CoVs, it might repress the replication of other viral families. First, we tested the effect of

293 PARP14 deletion on HSV-1, which has been co-evolving with humans for several million years.
294 Furthermore, PARP14 was identified as a host factor that binds to HSV-1 DNA [26, 27]. We
295 infected A549 WT and two different clones of PARP14 KO cells [3] with HSV-1 (strain KOS) at
296 a low MOI (0.01PFU/mL) and found that replication of HSV-1 was enhanced by over 2-logs
297 throughout the infection in PARP14 KO cells, strongly indicating that PARP14 represses HSV-1
298 replication **(Fig. 6A)**. HSV-1 infection is characterized by activation of some of its immediate
299 early genes like ICP0, ICP4 and ICP27. As a separate measure of replication, we infected WT and
300 KO cells with 0.1 MOI HSV-1 and quantified the expression of ICP0, ICP4 and ICP27 mRNA
301 transcripts at 24 hpi. We observed increased gene expression in PARP14 KO cells compared to
302 WT cells, again indicating that PARP14 restricts HSV-1 infection **(Fig. 6B).** We then corroborated
303 this observation by quantifying ICP0, ICP4 and ICP27 mRNA levels in A549 cells infected with
304 HSV-1 and treated with PARP14 degron (DEG) or its corresponding negative control (CTL).
305 Again, we saw an increase in the transcripts in DEG treated cells, confirming that the observed
306 increase in expression of ICP genes was due to the absence of PARP14 **(Fig. 6C)**. Next, we tested
307 the ability of HSV-1 to form plaques on A549 WT and PARP14 KO cells using a plaquing
308 efficiency assay. Similar to previous observations, we found that PARP14 KO also enhanced the
309 plaquing efficiency of HSV-1 compared to WT cells by >2-logs on average **(Fig. 6D)**. Since the
310 MARylating activity of PARP14 was responsible for restricting CoV replication we tested the
311 ability of PARP14i to enhance HSV-1 infection. Interestingly, HSV-1 replication was not affected
312 in PARP14i treated A549 cells compared to untreated cells, suggesting that PARP14 restricted
313 HSV-1 replication in a MARylation-independent manner **(Fig. 6E)**. Overall, these data show that
314 PARP14 restricts HSV-1 infection and does so in an ADP-ribosylation independent manner.

315 **PARP14 promotes the replication of vesicular stomatitis virus (VSV).**

316 Next, we tested the ability of PARP14 to restrict the replication of additional types of RNA
317 viruses. First, we tested the infectivity of lymphocytic choriomeningitis virus clone-13 (LCMV-
318 cl13), an ambisense RNA virus, in WT and PARP14 KO BMDMs. To measure infectivity of
319 LCMV-cl13 in BMDMs, we measured the amount of LCMV nucleoprotein (LCMV-NP) using a
320 fluorescently labeled antibody against LCMV-NP (clone anti-VL4) and intracellular flow
321 cytometry. PARP14 KO cells had comparable levels of LCMV-NP+ cells compared to WT cell,
322 ~4-5%. These data indicate that LCMV-cl13 infection is not impacted by PARP14 **(Fig. S3A-B)**.
323 To further explore the role of PARP14 in the replication of negative-sense RNA viruses, we tested
324 the ability of VSV-GFP to replicate in PARP14 KO A549 cells. Interestingly, VSV-GFP
325 replication was significantly reduced by in A549 PARP14 KO cells compared to WT cells,
326 indicating that PARP14 promotes VSV-GFP replication **(Fig. 7A)**. To confirm this result, we
327 created a new set of A549 WT and PARP14 KO cells using separate control and PARP14 targeting
328 guide RNAs **(Fig. S4)**. Again, we found that VSV replication was significantly reduced in these
329 cells **(Fig. 7B)**. Furthermore, the addition of the PARP14 degrader (DEG) significantly reduced
330 the replication of VSV in WT cells, while the CTL compound had no effect **(Fig. 7B)**. To
331 determine if these differences could be due to an increase in IFN-levels, we measured the level of
332 IFN following infection with VSV in both PARP14 KO and PARP14i treated cells. We
333 consistently found no substantial differences in IFN production following VSV infection in
334 PARP14 depleted cells **(Fig. S5A)**. To further confirm that there was no impact of IFN on virus
335 replication, we treated A549 cells with a JAK inhibitor (JAKi) that has previously been used to
336 ablate the production of ISGs [28, 29]. While the JAKi significantly reduced the levels of PARP14,
337 an ISG **(Fig. S5B)**, it did not lead to increased replication of VSV in WT or PARP14 KO cells
338 **(Fig. S5C)**. Finally, we tested whether the ADP-ribosyltransferase activity of PARP14 supported

339 VSV replication by treating A549 WT cells with PARP14i. PARP14i treatment did not
340 significantly reduce VSV replication, indicating that the proviral function of PARP14 was largely
341 independent of its MARylating activity **(Fig. 7C)**. Overall, these results suggest that PARP14 can
342 inhibit the replication of CoVs and HSV-1 but enhances the replication of VSV, a negative-sense
343 RNA virus.

344 **DISCUSSION**

345 PARP14 has emerged as a critical host factor that impacts multiple immune signaling pathways.
346 It was initially found to bind STAT6 and promote IL4-dependent anti-inflammatory gene
347 regulation [15]. This function of PARP14 promotes T_H2 gene expression and IgE production in
348 immune cells [30]. Recently, a PARP14 inhibitor (RBN-3143) was reported to mitigate the effects
349 of allergen-induced IgE production and overproduction of mucus, reduced T_H2 cell abundance and
350 restored αPD-1 sensitivity to tumors [31]. PARP14 also inhibits STAT-1 phosphorylation by
351 MARylating key residues, and knockdown or knockout of PARP14 increased pro-inflammatory
352 cytokines in primary human and mouse M1, but not M2 macrophages [16]. In contrast, PARP14
353 promoted IFN-I and pro-inflammatory cytokine production in RAW 264.7 cells following LPS
354 treatment and *S. typhimurium* infection [17]. PARP14 also promoted IFN-I production in response
355 to MHV infection and poly(I:C) stimulation in BMDMs and A549 cells, respectively [3]. In this
356 study, we demonstrated that the enzymatic activity of PARP14 promotes MDA5-dependent IFN-
357 I and IFN-III production when stimulated with a dsRNA analog poly(I:C), EMCV, or CoV
358 infection by directly quantifying IFN-I and IFN-III mRNA and protein levels in multiple cell lines.
359 In general, the impact of PARP14 on innate and adaptive immune pathways is cell type and
360 condition specific. It remains unclear if PARP14 both enhances IFN-I and IFN-III production and
361 limits IFN signaling in the same cells, or if it only represses IFN signaling in M1 macrophages. It

362 is feasible that PARP14 may dampen IFN signaling to control its own ability to stimulate IFN
363 production. How PARP14 regulates MDA-5-dependent IFN production and the broader impacts
364 of these functions remains unclear and is an active topic of research.

365 In addition to inducing IFN, PARP14 expression is stimulated by IFNs and virus infections
366 and that its ADP-ribosyltransferase activity triggers the production of IFN-induced ADP-ribose
367 bodies (ICABs) [3]. ICABs are regions of the cytoplasm with punctate ADP-ribose signal that has
368 been observed by immunofluorescence following IFN-γ or poly(I:C) treatment [18-21, 32]. In
369 addition, increased mono-ADP-ribosylation is visible by Western blotting following the same
370 treatments in A549 cells [18]. Importantly both signals were dependent on the catalytic activity of
371 PARP14 and can be reversed by macrodomain proteins, including the SARS-CoV-2 Mac1 protein
372 [18, 32]. These bodies also contain PARP9, DTX3L, and p62, and also overlap with ubiquitin
373 staining. Furthermore, DTX3L and p62 are ADP-ribosylated by PARP14, likely within ICABs,
374 and are required for the maintenance of the ICABs [18, 20, 21, 33]. Despite this, there is no current
375 data showing that PARP14 restricts virus infection. Here, we found that the catalytic activity of
376 PARP14 was required to repress the replication of Mac1-mutant CoVs. Furthermore, our findings
377 that PARP14 catalytic activity is required for the repression of SARS-CoV ΔMac1 only in the
378 presence of IFN-γ strongly suggests that ICABs play a key role in the repression of CoV
379 replication. Future studies will determine if p62, DTX3L, or other PARP14 targets within ICABs
380 participate in the restriction of CoV replication and the mechanisms by which they do so.

381 PARP14 is one of 4 PARPs that has evolved under positive selection, further indicating
382 that it is likely involved in host-pathogen conflict [22]. In addition to restricting Mac1-mutant
383 CoVs, we also found that it was required for repression of HSV-1. HSV-1 and other herpesviruses
384 have been evolving with mammals for millions of years, so it is maybe more likely that PARP14

385 is co-evolving with herpesviruses than CoVs. Finally, we found that PARP14 enhances the
386 replication of VSV in an ADP-ribosylation independent manner. PARP14 has been shown to
387 interact with SARS-CoV-2 RNA [35] and HSV-1 DNA [26], thus the mechanism by which
388 PARP14 restricts and promotes virus replication could be through interactions with nucleic acids.
389 In fact, PARP14 bound to the HSV-1 genome, in association with other DNA repair proteins, as
390 early as 3 hours post-infection, suggesting that PARP14 possibly binds to DNA to inhibit
391 transcription and/or DNA replication [26, 27]. These interactions may help explain the positive
392 selection of PARP14 as it may need to rapidly evolve to mutations in DNA or RNA sequences
393 within viral genomes.

394 PARP14 is a large protein (203kDa) with multiple domains [12]. The ADP-ribosyl
395 transferase (ART) domain of PARP14 binds to NAD^+ and transfers an ADP-ribose moiety to its
396 targets. Its ART domain has an HYL (hydrophobic residue-tyrosine-leucine) domain as part of the
397 catalytic triad, which restricts its ART activity to MARylation [36, 37]. PARP14 also has 3 tandem
398 macrodomains (MD), of which MD1 has ADP-ribosylhydrolase (ARH) activity against
399 MARylated protein and nucleic acid substrates, making it a rare enzyme that both adds and
400 reverses the same post-translational modification [13, 14]. PARP14 also has a WWE domain that
401 can bind to ADP-ribose subunits [38], several KH domains that facilitate protein and nucleic acid
402 binding, and several RNA recognition motifs (RRMs) [12]. However, the roles and substrates of
403 these domains, especially during virus infection, remain largely unknown. Given the potential of
404 PARP14 to bind and modify protein and nucleic acid substrates through its many domains,
405 identifying the protein and/or nucleic acid binding partners of PARP14 during infection and the
406 domains required for these interactions could reveal several novel mechanisms by which PARP14
407 regulates virus replication and pathogenesis.

408 **MATERIALS AND METHODS**

409 **Biosafety statements**

410 All work with SARS-CoV-2 was conducted in the University of Kansas EHS-approved BSL-3
411 facility following standard operating procedures. All work with wild-type and recombinant Ebola
412 virus and Nipah virus was performed in the biosafety level 4 (BSL-4) facility of Boston
413 University's National Emerging Infectious Diseases Laboratories (NEIDL) following approved
414 standard operating procedures in compliance with local and national regulations pertaining to
415 handling BSL-4 pathogens and Select Agents. Animal studies were approved by the Institutional
416 Animal Care and Use Committees at the University of Iowa and the University of Kansas and met
417 stipulations of the Guide for the Care and Use of Laboratory Animals.

418 **Cell culture and reagents**

419 NHDF, 293T, Hela-MVR, A549, A549-PARP14KO, A549-ACE2 (a generous gift from Susan
420 Weiss, University of Pennsylvania), BHK, 17Cl-1, and Vero E6 cells were grown in Dulbecco's
421 modified Eagle medium (DMEM) supplemented with 10% fetal bovine serum (FBS). Calu-3 cells
422 (ATCC) were grown in MEM supplemented with 20% FBS. Baby hamster kidney cell line BSR-
423 T7/5 constitutively expressing T7 RNA polymerase was maintained in Glasgow's Minimum
424 Essential Medium (G-MEM) with 10% FBS. Bone marrow derived cells were grown in RPMI
425 supplemented with 10% FBS and differentiated into M0 macrophages using M-CSF (Millipore-
426 Sigma) and dendritic cells (DCs) using GM-CSF (Millipore-Sigma). All cell lines were grown at
427 37°C and 5% CO_2. IFN-γ was purchased from R&D Systems and Poly(I:C) HMW (0.5µg/mL)
428 was purchased from Millipore-Sigma. RBN012759 (PARP14i) was purchased from Atomwise.
429 RBN012811 (DEG) and its associated negative control RBN013527 (CTL) were generously
430 provided by Dr. Mario Niepel (Ribon Therapeutics). Cells were transfected with either Polyjet

431 (Amgen), Lipofectamine 3000 (Fisher Scientific), or jetOPTIMUS (Polyplus) per the
432 manufacturer's instructions.

433 **Creation of inducible PARP14 knock-out mice**

434 *Animals.* The insertion of loxP sites flanking exon 2 of PARP14 was carried out by the University
435 of Iowa genome editing facility. C57BL/6J mice were purchased from Jackson Labs (000664; Bar
436 Harbor, ME). Male mice older than 8 weeks were used to breed with 3-5-week-old super-ovulated
437 females to produce zygotes for pronuclear injection. Female ICR (Envigo; Hsc:ICR(CD-1)) mice
438 were used as recipients for embryo transfer. All animals were maintained in a climate-controlled
439 environment at 25°C and a 12/12 light/dark cycle.

440 *Preparation of Cas9 RNPs and the injection mix.* Chemically modified CRISPR-Cas9 crRNAs
441 targeting regions 5' and 3' of exon 2 of PARP14 **(Table S1)** and CRISPR-Cas9 tracrRNA were
442 purchased from IDT (Alt-R® CRISPR-Cas9 crRNA; Alt-R® CRISPR-Cas9 tracrRNA (Cat#
443 1072532)). The crRNAs and tracrRNA were suspended in T10E0.1 and combined to 1 ug/ul (~29.5
444 uM) final concentration in a 1:2 (µg:µg) ratio. The RNAs were heated at 98°C for 2 min and
445 allowed to cool slowly to 20°C in a thermal cycler. The annealed cr:tracrRNAs were aliquoted to
446 single-use tubes and stored at -80°C. Cas9 nuclease was also purchased from IDT (Alt-R® S.p.
447 HiFi Cas9 Nuclease). Cr:tracr:Cas9 ribonucleoprotein complexes were made by combining Cas9
448 protein and cr:tracrRNA in T10E0.1 (final concentrations: 250 ng/μl (~1.6 μM) Cas9 protein and
449 200 ng/μl (~6.1 μM) cr:tracrRNA). The Cas9 protein and annealed RNAs were incubated at 37°C
450 for 10 minutes. The RNP complexes were combined with single-stranded repair template,
451 containing the loxP sites to be inserted around exon2, and incubated an additional 5 minutes at
452 37°C (single-stranded repair template sequence available upon request). The concentrations in the

453 injection mix were 50 ng/μl (~0.3 μM) Cas9 protein and 20 ng/μl (~0.6 μM) each cr:tracrRNA and
454 40 ng/μl single-stranded repair template.
455 *Collection of embryos and injection.* Pronuclear-stage embryos were collected using methods
456 described in [39]. Embryos were collected in KSOM media (Millipore; MR101D) and washed 3
457 times to remove cumulous cells. Cas9 RNPs and double-stranded repair template were injected
458 into the pronuclei of the collected zygotes and incubated in KSOM with amino acids at 37°C under
459 5% CO_2 until all zygotes were injected. The CRISPR injection protocol was previously
460 described[40]. Fifteen to 25 embryos were immediately implanted into the oviducts of pseudo-
461 pregnant ICR females. Offspring were heterozygote for the loxP insertions. These mice were
462 sequentially bred to result in floxed homozygote mice. Genotyping was performed using PCR
463 amplification with primers listed in **Table S2**. and restriction digestion by EcoR1. These were then
464 crossed with C57BL/6.Cg-Ndor1$^{Tg(UBC\text{-}cre/ERT2)1Ejb}$/IJ mice (Jax strain # 007001) till mice colonies
465 that were homozygous for *loxP* sites and heterozygous for *cre* gene were confirmed by genotyping.
466 The resulting mice were backcrossed twice before using these mice for the experiments described
467 in this study.
468 **Creation of PARP14 knock-out A549-ACE2 cells**
469 A549-ACE2 cells were cultured in DMEM supplemented with 10% FBS at 37°C with 5% CO_2.
470 For CRISPR/Cas9 transfection, cells were seeded in 6-well plates at 2×10^5 cells per well, before
471 transfection. At 40-80% confluency, cells were transfected with either PARP14 CRISPR/Cas9 KO
472 plasmid (sc-402812, Santa Cruz Biotechnology) or control CRISPR/Cas9 plasmid (sc-418922,
473 Santa Cruz Biotechnology) using PolyJet transfection reagent according to manufacturer's
474 instructions. After 72 hours of incubation, successful transfection was confirmed by GFP
475 expression via fluorescence microscopy. GFP-positive cells were isolated using a BD

476 FACSymphony cell sorter, and single cells were sorted into individual wells to establish
477 monoclonal populations. WT control and PARP14 knockout expanded clones were validated by
478 Western blot analysis using anti-PARP14 mouse monoclonal antibody (sc-377150, Santa Cruz
479 Biotechnology).

480 **Virus infections**

481 *MHV-JHM^{IA}*. Recombinant WT and N1347A MHV JHM^{IA} virus used in this study have been
482 previously reported [3, 41, 42]. Virus stocks were grown in 17Cl-1 cells and titered by plaque
483 assay in Hela-MVR cells. BMDMs and DCs were infected at an MOI of 0.1 PFU/cell for indicated
484 periods of times after a 60-min adsorption phase. Virus titers were determined by plaque assay on
485 Hela-MVR cells.

486 *SARS-CoV-2*. Recombinant SARS-CoV-2 WT and ΔMac1 virus based on the original Wuhan
487 isolate used in this study has been previously reported [25]. Virus stocks were grown and titered
488 by plaque assay in VeroE6 cells. A549-ACE2 cells were infected at an MOI of 0.1 for 48 hours
489 after a 60-min adsorption phase. Calu3 cells were infected at an MOI of 0.1 for 48 hours after a
490 120-min adsorption phase and Trypsin-TCPK treatment (1μg/mL). Virus titers were determined
491 in Vero E6 cells using plaque assay. All the SARS-CoV-2 experiments were carried out under
492 BSL-3 conditions at the University of Kansas, following approved SOPs.

493 *HSV-1.* Stocks of HSV-1 strain KOS was propagated and titered as previously described [43]. For
494 viral yield assays, A549 and A549-PARP14KO cells (5×10^4) were seeded in triplicate in a 24-well
495 plate and infected at an MOI of 0.1 PFU/cell with HSV-1. At 1 hpi, cells were washed twice with
496 PBS to remove unabsorbed virus. Infected cells were harvested and collected 24 hpi and titered by
497 standard plaque assays on Vero cells. For PARP14 inhibitor experiments, A549 cells were treated
498 with or without PARP14 inhibitor, and infections were carried out as described for the HSV-1

499 yield assays. To determine plaquing efficiencies, A549 and A549-PARP14KO cells were plated
500 in triplicate in 12-well plates and infected with serial dilutions from HSV-1 stocks, and titers were
501 determined by standard plaque assays. To assess virus transcript levels, A549 cell lines (5×10^4)
502 were plated in triplicate in a 24-well plate. Cells were infected at an MOI of 0.1 with HSV-1 and
503 washed twice with PBS 1 hpi. At 6 hpi, media were removed, and cells were resuspended in TRIzol
504 reagent (250 μL). RNA was isolated according to manufacturer's protocol and reverse transcribed
505 as published (ref). cDNAs of viral and cellular transcripts were amplified using primers for ICP0,
506 ICP4, ICP27, and 18S rRNA as previously described [44].
507 *VSV*. VSV-GFP Indiana strain was generously provided by Dr. Asit Pattnaik (University of
508 Nebraska-Lincoln) [45]. Virus stocks were grown and titered by plaque assay in VeroE6 cells.
509 A549 cells were infected with VSV-GFP at an MOI of 1 PFU/cell. Infected cells were then
510 incubated and collected at 10 hpi after a 60-min adsorption phase. Virus titer was determined by
511 50% tissue culture infectious dose ($TCID_{50}$) assay in Vero E6 cells.
512 *LCMV*. LCMV Clone-13 (LCMV-cl13) virus stocks were grown in BHK cells and titered by
513 plaque assay in Vero E6 cells. BMDM cells were infected with LCMV-cl13 at an MOI of 2-6.
514 Infected cells were then incubated and collected at 24 hpi. For surface staining, samples were
515 treated with Fc block (CD16/32, eBioscience) and then incubated with Tonbo Ghost Viability dye
516 (violet 510, Tonbo biosciences), F4/80 (Pacific orange, Invitrogen, CLONE) and LCMV-NP
517 (clone VL4 (BioXcell), self-conjugated to Alexa Fluor 488 following manufacturer's instructions,
518 (Thermo Fisher Scientific)). All flow cytometry data were analyzed using FlowJo software (BD
519 Biosciences).
520 **Immunoblotting**

521 Total cell extracts were lysed in sample buffer containing SDS, protease and phosphatase
522 inhibitors (Roche), β-mercaptoethanol, and a universal nuclease (Fisher Scientific) and boiled at
523 95ºC for 5 minutes. Proteins were resolved on an SDS polyacrylamide gel, transferred to a
524 polyvinylidene difluoride (PVDF) membrane, hybridized with a primary antibody, reacted with an
525 infrared (IR) dye-conjugated secondary antibody, visualized using a Li-COR Odyssey Imager (Li-
526 COR), and analyzed using Image Studio software. Primary antibodies used for immunoblotting
527 included anti-SARS-CoV-2 N (SinoBiological 40143-R001, 1:5000), anti-OAS3 (Cell Signaling
528 41440, 1:250), anti-PARP14 (Santa Cruz Biotechnology SC-377150, 1:100), and anti-GAPDH
529 (Millipore-Sigma G8795, 1:5000) antibodies. Secondary IR antibodies were purchased from Li-
530 COR.

531 **PARP14 cellular ADP-ribosylation assays**

532 293T cells were transfected with GFP-PARP14 WT or GFP-PARP14 G832E plasmid using the
533 jetOPTIMUS transfection reagent with 0.4 µg DNA/well and with a ratio of 1:1 µL transfection
534 reagent: µg DNA. The media was exchanged 4 hours post-transfection. The next day, cells were
535 dosed with RBN012759 for 4 hours. Cells were washed once with cold PBS and the plate was
536 frozen at -80ºC prior to lysis. Samples were thawed on ice, lysed with a cytosolic lysis buffer [50
537 mM HEPES pH 7.4, 150 mM NaCl, 1 mM $MgCl_2$, 1% tritonX-100 supplemented with fresh 1 mM
538 TCEP, 1X cOmplete EDTA-free Protease Inhibitor Cocktail (Roche) and 30 µM Phthal01
539 (panPARP inhibitor) [46]], and clarified by centrifugation at 14,000 rpm at 4ºC for 10 minutes.
540 The supernatant containing total protein was quantified using the Bradford assay reagent (Bio-
541 Rad). Lysates were normalized and sample buffer was added to 1X (10% glycerol, 50mM Tris-Cl
542 (pH 6.8), 2% SDS, 1% β-mercaptoethanol, 0.02% bromophenol blue). Samples were boiled at
543 95ºC for 5 min and resolved in 4-20% Mini-PROTEAN® TGX™ Precast Protein Gels (Bio-Rad).

544 Proteins were transferred to a nitrocellulose membrane and probed overnight at 4ºC with primary
545 antibodies, followed by incubation with goat anti-rabbit (1:10000, Jackson Immuno Reseach Labs)
546 or goat anti-mouse (1:5000, Invitrogen) HRP-conjugated secondary antibodies. The blots were
547 then incubated SuperSignal™ West Pico substrate (Thermo Scientific) and imaged on a ChemiDoc
548 Gel Imaging System (Bio-Rad). Primary antibodies used for this experiment were: Poly/Mono-
549 ADP ribose antibody (Cell Signaling Technology, E6F6A, 1:2000), Tubulin (Cell Signaling
550 Technology, DM1A, 1:2000), GFP (Proteintech, pabg1, 1:1000), Mono-ADP-Ribose antibody
551 33204 (Bio-Rad, HCA354, 2 µg/ml), and PARP14 (Millipore Sigma, HPA012063, 1:1000).

552 **Real-Time (RT-qPCR) Analysis**

553 RNA was isolated from respective cells using Trizol (Invitrogen). Briefly, cells were collected at
554 indicated time points in Trizol (Invitrogen) and RNA was isolated as per manufacturer's
555 instructions. cDNA was prepared using M-MuLV-reverse transcriptase per the manufacturer's
556 instructions (NEB). qPCR was performed using PowerUp SYBR green master mix (Applied
557 Biosystems) and primers listed in **Table S3**. Cycle threshold values were normalized to
558 hypoxanthine phosphoribosyltransferase (HPRT), glyceraldehyde-3-phosphate dehydrogenase
559 (GAPDH), or 18S rRNA levels using the ΔCt method.

560 **RNAseq**

561 RNA was isolated from infected BMDMs with and without treatment, isolated from C57BL6 mice
562 as described above. Library preparation with indexing was performed by the University of Kansas
563 Genome Sequencing core facility with NEB Next RNA Library kit (NEB). RNAseq was
564 performed using an Illumina NextSeq2000 high-output system with paired-end reads of 50 bp.
565 DESeq2 was used to identify DEGs between the BMDM without treatment and MHV-JHM
566 N1347A infected and BMDM with 100nM PARP14 inhibitor treatment and N1347A infected

567 samples using simply "treatment" as a factor. DEGs were identified based on the false-discovery
568 rate corrected *P*-value (P_{ADJ}) and log_2-fold-change of (log_2FC) between the samples. Genes were
569 considered up-regulated in an MHV-JHM-infected sample if $P_{ADJ} < 0.05$ and $log_2FC > 0.6$, which
570 is nearly equivalent to a 1.5-fold increase. Similarly, genes were considered down-regulated if
571 $P_{ADJ} < 0.05$ and $log_2FC < -0.6$, or a 1.5-fold decrease. DEGs were subjected to gene ontology
572 analysis using the Database for Annotation, Visualization and Integrated Discovery
573 (DAVID: https://david.ncifcrf.gov/).

574 **Primers**

575 Primers were used at 10μM concentration and the primers sequences for human HPRT, IFNβ,
576 GAPDH [47], CXCL10 and mouse HPRT, IFNβ and ISG15 have been previously published [25].
577 RNAseq data was corroborated by qPCR using primer sequences CASP1F
578 TACACGTCTTGCCCTCATTATC, CASP1R CTCCAGCAGCAACTTCATTTC, FOXO3F
579 TTTCCTACGTCTCCTGCTAATG, FOXO3R CTCCTTAGGCTGACGCTAATC, RNF111F
580 CGACTTCATCACCTCCAGTTAG, RNF111R GCTCCATCCAATCCTGAAGAA. Dentritic
581 cell verification was done using qPCR using the primers CXCR1F
582 TTCCCATCTGCTCAGGACCTC and CXCR1R ATTTCCCACCAGACCGAACG.

583 **Immunofluorescence Analysis and Imaging**

584 Immunofluorescence to detect NiV was performed as described as follows. Briefly, formalin-fixed
585 cells were washed 4 times with phosphate-buffered saline (PBS), permeabilized with a mixture of
586 acetone and methanol (1:1, *v*/*v*) for 5 min at −20 °C, washed 4 times with PBS, treated with 0.1 M
587 glycine for 5 min at room temperature, washed 4 times with PBS, and then incubated in blocking
588 solution (2% bovine serum albumin, 0.2% Tween 20, 3% glycerol, and 0.05% sodium azide in
589 PBS) for 1 h at room temperature. The primary antibody used for the detection of NiV (mouse

590 hyperimmune ascitic fluid diluted 1:500 in blocking solution, BEI NR-48961) was added and
591 incubated overnight at 4°C. Cells were washed 4 times with PBS and then incubated with
592 secondary antibody (goat α-mouse AlexaFluor 488 diluted 1:100 in blocking solution, Invitrogen)
593 in the presence of 4′,6-diamidino-2-phenylindole (DAPI; 200 ng/mL). rEBOV-ZsG-infected cells
594 were stained with DAPI (200 ng/mL). Infections and immunofluorescence analyses were
595 performed three times in independent experiments.
596 Samples were imaged at 4x magnification on a Nikon Ti2 Eclipse inverted fluorescent microscope
597 and Photometrics Prime BSI camera using NIS Elements AR software. One representative image
598 from each well, covering an area of 10.87 mm^2, was collected for quantification.
599 **Statistics.** A Student's *t* test or one-way ANOVA were used to analyze differences in mean
600 values between groups. All results are expressed as means ± standard errors of the means (SEM).
601 P values of ≤0.05 were considered statistically significant (*, P≤0.05; **, P≤0.01; ***, P≤0.001;
602 ****, P ≤0.0001; n.s., not significant). "ns" stands for data with P value >0.05 and hence is not
603 significant. Fold changes are designated by a number followed by X above the significance
604 values.
605 **Data and materials availability.** All the RNAseq reads data will be deposited in NCBI
606 (Bioproject ID: PRJNA1139810; Biosample ID: SAMN42785804 (DMSO) and
607 SAMN42786772(PARP14 inhibitor treatment)) and will be made public upon acceptance. All
608 other data will be available through FigShare at the time of acceptance.
609 10.6084/m9.figshare.c.7766243

ACKNOWLEDGMENTS

We thank members of the Davido and Orozco labs for valuable discussion. We thank Stanley Perlman, Susan Weiss, Mario Niepel, Asit Pattnaik, and Heinz Feldmann for reagents. Bioinformatic consultation was provided by the KU Center for Genomics. Research reported in this publication was made possible in part by the services of the KU Genome Sequencing Core which is supported by NIH/NIGMS under grant award number P30GM145499, and the KU Flow Cytometry Core, which is supported in part by the NIH/NIGMS under grant award number P20GM113117. Transgenic mice were generated at the University of Iowa Genome Editing Core Facility directed by William Paradee, PhD and supported in part by grants from the NIH and from the Roy J. and Lucille A. Carver College of Medicine. We wish to thank Norma Sinclair, Patricia Yarolem, Joanne Schwarting and Rongbin Guan for their technical expertise in generating transgenic mice. We also thank Mitchell White (Boston University) for excellent technical assistance.

Funding:
National Institutes of Health (NIH) grant P20GM113117 (ARF & RCO)
National Institutes of Health (NIH) grant K22AI134993 (ARF)
National Institutes of Health (NIH) grant R35GM138029 (ARF)
National Institutes of Health (NIH) grant R01AI123231 (CSS)
National Institutes of Health (NIH) grant R01HL126901 (MA)
National Institutes of Health (NIH) grant R01AI133486 (EM)
National Institutes of Health (NIH) grant R21AI169646 (EM)
National Institutes of Health (NIH) grant UC7 AI070088 (EM)
Bill & Melinda Gates Foundation grant INV-048926 (EM)

Author contributions:
Conceptualization: SP, ARF
Methodology: SP, ELS, DSB, NS, MA, RCO, CSS, MSC, DJD, AJH, ARF
Investigation: SP, PS, HH, AF, JJP, ELS, DSB, YC, NS, RCO, CSS, DJD, AJH, ARF
Visualization: SP, PS, HH, AF, JJP, ELS, DSB, YC, RCO, CSS, MSC, DJD, AJH, ARF
Supervision: SP, EM, RCO, CSS, MSC, DJD, AJH, ARF
Writing—original draft: SP, ARF
Writing—review & editing: SP, PS, HH, AF, JJP, ELS, DSB, YC, NS, JA, EM, RCO, CSS, MSC, DJD, AJH, ARF

Competing interests: A.R.F. was named as an inventor on a patent filed by the University of Kansas for a live-attenuated SARS-CoV-2 vaccine.

649 **REFERENCES**

650 1. Luscher B, Ahel I, Altmeyer M, Ashworth A, Bai P, Chang P, et al. ADP-ribosyltransferases, an
651 update on function and nomenclature. FEBS J. 2022;289(23):7399-410. Epub 20210913. doi:
652 10.1111/febs.16142. PubMed PMID: 34323016; PubMed Central PMCID: PMCPMC9027952.
653 2. Rack JG, Perina D, Ahel I. Macrodomains: Structure, Function, Evolution, and Catalytic Activities.
654 Annu Rev Biochem. 2016;85:431-54. Epub 2016/02/05. doi: 10.1146/annurev-biochem-060815-
655 014935. PubMed PMID: 26844395.
656 3. Grunewald ME, Chen Y, Kuny C, Maejima T, Lease R, Ferraris D, et al. The coronavirus
657 macrodomain is required to prevent PARP-mediated inhibition of virus replication and enhancement
658 of IFN expression. PLoS Pathog. 2019;15(5):e1007756. Epub 2019/05/17. doi:
659 10.1371/journal.ppat.1007756. PubMed PMID: 31095648; PubMed Central PMCID:
660 PMCPMC6521996.
661 4. Alhammad YM, Parthasarathy S, Ghimire R, O'Connor JJ, Kerr CM, Pfannenstiel JJ, et al. SARS-
662 CoV-2 Mac1 is required for IFN antagonism and efficient virus replication in mice. bioRxiv. 2023.
663 Epub 20230406. doi: 10.1101/2023.04.06.535927. PubMed PMID: 37066301; PubMed Central
664 PMCID: PMCPMC10104158.
665 5. Fehr AR, Channappanavar R, Jankevicius G, Fett C, Zhao J, Athmer J, et al. The Conserved
666 Coronavirus Macrodomain Promotes Virulence and Suppresses the Innate Immune Response during
667 Severe Acute Respiratory Syndrome Coronavirus Infection. mBio. 2016;7(6). Epub 20161213. doi:
668 10.1128/mBio.01721-16. PubMed PMID: 27965448; PubMed Central PMCID: PMCPMC5156301.
669 6. Brady PN, Goel A, Johnson MA. Correction for Brady et al., "Poly(ADP-Ribose) Polymerases in
670 Host-Pathogen Interactions, Inflammation, and Immunity". Microbiol Mol Biol Rev. 2019;83(2).
671 Epub 20190313. doi: 10.1128/MMBR.00010-19. PubMed PMID: 30867231; PubMed Central
672 PMCID: PMCPMC6684004.
673 7. Guo T, Zuo Y, Qian L, Liu J, Yuan Y, Xu K, et al. ADP-ribosyltransferase PARP11 modulates the
674 interferon antiviral response by mono-ADP-ribosylating the ubiquitin E3 ligase beta-TrCP. Nat
675 Microbiol. 2019;4(11):1872-84. Epub 20190415. doi: 10.1038/s41564-019-0428-3. PubMed PMID:
676 30988430.
677 8. Yamada T, Horimoto H, Kameyama T, Hayakawa S, Yamato H, Dazai M, et al. Constitutive aryl
678 hydrocarbon receptor signaling constrains type I interferon-mediated antiviral innate defense. Nat
679 Immunol. 2016;17(6):687-94. Epub 20160418. doi: 10.1038/ni.3422. PubMed PMID: 27089381.
680 9. Grady SL, Hwang J, Vastag L, Rabinowitz JD, Shenk T. Herpes simplex virus 1 infection activates
681 poly(ADP-ribose) polymerase and triggers the degradation of poly(ADP-ribose) glycohydrolase. J
682 Virol. 2012;86(15):8259-68. Epub 20120523. doi: 10.1128/JVI.00495-12. PubMed PMID: 22623791;
683 PubMed Central PMCID: PMCPMC3421676.
684 10. Ha HC, Juluri K, Zhou Y, Leung S, Hermankova M, Snyder SH. Poly(ADP-ribose) polymerase-1 is
685 required for efficient HIV-1 integration. Proc Natl Acad Sci U S A. 2001;98(6):3364-8. Epub
686 20010306. doi: 10.1073/pnas.051633498. PubMed PMID: 11248084; PubMed Central PMCID:
687 PMCPMC30659.
688 11. Tempera I, Deng Z, Atanasiu C, Chen CJ, D'Erme M, Lieberman PM. Regulation of Epstein-Barr
689 virus OriP replication by poly(ADP-ribose) polymerase 1. J Virol. 2010;84(10):4988-97. Epub
690 20100310. doi: 10.1128/JVI.02333-09. PubMed PMID: 20219917; PubMed Central PMCID:
691 PMCPMC2863838.
692 12. Suskiewicz MJ, Munnur D, Stromland O, Yang JC, Easton LE, Chatrin C, et al. Updated protein
693 domain annotation of the PARP protein family sheds new light on biological function. Nucleic Acids
694 Res. 2023;51(15):8217-36. doi: 10.1093/nar/gkad514. PubMed PMID: 37326024; PubMed Central
695 PMCID: PMCPMC10450202.
696 13. Delgado-Rodriguez SE, Ryan AP, Daugherty MD. Recurrent Loss of Macrodomain Activity in Host
697 Immunity and Viral Proteins. Pathogens. 2023;12(5). Epub 20230503. doi:

10.3390/pathogens12050674. PubMed PMID: 37242344; PubMed Central PMCID: PMCPMC10221186.

14. Dukic N, Stromland O, Elsborg JD, Munnur D, Zhu K, Schuller M, et al. PARP14 is a PARP with both ADP-ribosyl transferase and hydrolase activities. Sci Adv. 2023;9(37):eadi2687. Epub 2023/09/13. doi: 10.1126/sciadv.adi2687. PubMed PMID: 37703374; PubMed Central PMCID: PMCPMC10499325.
15. Goenka S, Boothby M. Selective potentiation of Stat-dependent gene expression by collaborator of Stat6 (CoaSt6), a transcriptional cofactor. Proc Natl Acad Sci U S A. 2006;103(11):4210-5. Epub 20060306. doi: 10.1073/pnas.0506981103. PubMed PMID: 16537510; PubMed Central PMCID: PMCPMC1449672.
16. Iwata H, Goettsch C, Sharma A, Ricchiuto P, Goh WW, Halu A, et al. PARP9 and PARP14 cross-regulate macrophage activation via STAT1 ADP-ribosylation. Nat Commun. 2016;7:12849. Epub 2016/11/01. doi: 10.1038/ncomms12849. PubMed PMID: 27796300; PubMed Central PMCID: PMCPMC5095532.
17. Caprara G, Prosperini E, Piccolo V, Sigismondo G, Melacarne A, Cuomo A, et al. PARP14 Controls the Nuclear Accumulation of a Subset of Type I IFN-Inducible Proteins. J Immunol. 2018;200(7):2439-54. Epub 2018/03/04. doi: 10.4049/jimmunol.1701117. PubMed PMID: 29500242.
18. Kar P, Chatrin C, Dukic N, Suyari O, Schuller M, Zhu K, et al. PARP14 and PARP9/DTX3L regulate interferon-induced ADP-ribosylation. EMBO J. 2024;43(14):2929-53. Epub 20240604. doi: 10.1038/s44318-024-00126-0. PubMed PMID: 38834853; PubMed Central PMCID: PMCPMC11251020.
19. Ribeiro VC, Russo LC, Gonzalez Dure DM, Hoch NC. Interferon-induced ADP-ribosylation: technical developments driving ICAB discovery. Biosci Rep. 2025;45(3). Epub 20250314. doi: 10.1042/BSR20240986. PubMed PMID: 40014063.
20. Ribeiro VC, Russo LC, Hoch NC. PARP14 is regulated by the PARP9/DTX3L complex and promotes interferon gamma-induced ADP-ribosylation. EMBO J. 2024;43(14):2908-28. Epub 20240604. doi: 10.1038/s44318-024-00125-1. PubMed PMID: 38834852; PubMed Central PMCID: PMCPMC11251048.
21. Raja R, Biswas B, Abraham R, Wang Y, Chang CY, Hendriks IA, et al. Interferon-induced PARP14-mediated ADP-ribosylation in p62 bodies requires the ubiquitin-proteasome system. EMBO J. 2025. Epub 20250407. doi: 10.1038/s44318-025-00421-4. PubMed PMID: 40195501.
22. Daugherty MD, Young JM, Kerns JA, Malik HS. Rapid evolution of PARP genes suggests a broad role for ADP-ribosylation in host-virus conflicts. PLoS Genet. 2014;10(5):e1004403. Epub 2014/05/31. doi: 10.1371/journal.pgen.1004403. PubMed PMID: 24875882; PubMed Central PMCID: PMCPMC4038475.
23. Schenkel LB, Molina JR, Swinger KK, Abo R, Blackwell DJ, Lu AZ, et al. A potent and selective PARP14 inhibitor decreases protumor macrophage gene expression and elicits inflammatory responses in tumor explants. Cell Chem Biol. 2021;28(8):1158-68 e13. Epub 20210310. doi: 10.1016/j.chembiol.2021.02.010. PubMed PMID: 33705687.
24. Wigle TJ, Ren Y, Molina JR, Blackwell DJ, Schenkel LB, Swinger KK, et al. Targeted Degradation of PARP14 Using a Heterobifunctional Small Molecule. Chembiochem. 2021;22(12):2107-10. Epub 20210504. doi: 10.1002/cbic.202100047. PubMed PMID: 33838082.
25. Alhammad YM, Parthasarathy S, Ghimire R, Kerr CM, O'Connor JJ, Pfannenstiel JJ, et al. SARS-CoV-2 Mac1 is required for IFN antagonism and efficient virus replication in cell culture and in mice. Proc Natl Acad Sci U S A. 2023;120(35):e2302083120. Epub 2023/08/22. doi: 10.1073/pnas.2302083120. PubMed PMID: 37607224; PubMed Central PMCID: PMCPMC10468617.
26. Dembowski JA, DeLuca NA. Temporal Viral Genome-Protein Interactions Define Distinct Stages of Productive Herpesviral Infection. mBio. 2018;9(4). Epub 20180717. doi: 10.1128/mBio.01182-18. PubMed PMID: 30018111; PubMed Central PMCID: PMCPMC6050965.

27. Dembowski JA, Dremel SE, DeLuca NA. Replication-Coupled Recruitment of Viral and Cellular Factors to Herpes Simplex Virus Type 1 Replication Forks for the Maintenance and Expression of Viral Genomes. PLoS Pathog. 2017;13(1):e1006166. Epub 20170117. doi: 10.1371/journal.ppat.1006166. PubMed PMID: 28095497; PubMed Central PMCID: PMCPMC5271410.
28. Otter CJ, Bracci N, Parenti NA, Ye C, Asthana A, Blomqvist EK, et al. SARS-CoV-2 nsp15 endoribonuclease antagonizes dsRNA-induced antiviral signaling. Proc Natl Acad Sci U S A. 2024;121(15):e2320194121. Epub 20240403. doi: 10.1073/pnas.2320194121. PubMed PMID: 38568967; PubMed Central PMCID: PMCPMC11009620.
29. Otter CJ, Renner DM, Fausto A, Tan LH, Cohen NA, Weiss SR. Interferon signaling in the nasal epithelium distinguishes among lethal and common cold coronaviruses and mediates viral clearance. Proc Natl Acad Sci U S A. 2024;121(21):e2402540121. Epub 20240517. doi: 10.1073/pnas.2402540121. PubMed PMID: 38758698; PubMed Central PMCID: PMCPMC11127059.
30. Goenka S, Cho SH, Boothby M. Collaborator of Stat6 (CoaSt6)-associated poly(ADP-ribose) polymerase activity modulates Stat6-dependent gene transcription. J Biol Chem. 2007;282(26):18732-9. Epub 20070503. doi: 10.1074/jbc.M611283200. PubMed PMID: 17478423.
31. Wong CW, Evangelou C, Sefton KN, Leshem R, Zhang W, Gopalan V, et al. PARP14 inhibition restores PD-1 immune checkpoint inhibitor response following IFNgamma-driven acquired resistance in preclinical cancer models. Nat Commun. 2023;14(1):5983. Epub 20230926. doi: 10.1038/s41467-023-41737-1. PubMed PMID: 37752135; PubMed Central PMCID: PMCPMC10522711.
32. Russo LC, Tomasin R, Matos IA, Manucci AC, Sowa ST, Dale K, et al. The SARS-CoV-2 Nsp3 macrodomain reverses PARP9/DTX3L-dependent ADP-ribosylation induced by interferon signaling. J Biol Chem. 2021;297(3):101041. Epub 20210804. doi: 10.1016/j.jbc.2021.101041. PubMed PMID: 34358560; PubMed Central PMCID: PMCPMC8332738.
33. Kubon D, Leslie Pedrioli DM, Hottiger MO. PARP14 mediated SQSTM1/p62 cysteine ADP-ribosylation is counteracted by the SARS-CoV-2 macrodomain. bioRxiv. 2024:2024.06.29.601315. doi: 10.1101/2024.06.29.601315.
34. Alhammad YMO, Kashipathy MM, Roy A, Gagne JP, McDonald P, Gao P, et al. The SARS-CoV-2 Conserved Macrodomain Is a Mono-ADP-Ribosylhydrolase. J Virol. 2021;95(3). Epub 20210113. doi: 10.1128/JVI.01969-20. PubMed PMID: 33158944; PubMed Central PMCID: PMCPMC7925111.
35. Whitworth IT, Knoener RA, Puray-Chavez M, Halfmann P, Romero S, Baddouh M, et al. Defining Distinct RNA-Protein Interactomes of SARS-CoV-2 Genomic and Subgenomic RNAs. J Proteome Res. 2024;23(1):149-60. Epub 20231203. doi: 10.1021/acs.jproteome.3c00506. PubMed PMID: 38043095; PubMed Central PMCID: PMCPMC10804885.
36. Kleine H, Poreba E, Lesniewicz K, Hassa PO, Hottiger MO, Litchfield DW, et al. Substrate-assisted catalysis by PARP10 limits its activity to mono-ADP-ribosylation. Mol Cell. 2008;32(1):57-69. doi: 10.1016/j.molcel.2008.08.009. PubMed PMID: 18851833.
37. Wahlberg E, Karlberg T, Kouznetsova E, Markova N, Macchiarulo A, Thorsell AG, et al. Family-wide chemical profiling and structural analysis of PARP and tankyrase inhibitors. Nat Biotechnol. 2012;30(3):283-8. Epub 20120219. doi: 10.1038/nbt.2121. PubMed PMID: 22343925.
38. Wang Z, Michaud GA, Cheng Z, Zhang Y, Hinds TR, Fan E, et al. Recognition of the iso-ADP-ribose moiety in poly(ADP-ribose) by WWE domains suggests a general mechanism for poly(ADP-ribosyl)ation-dependent ubiquitination. Genes Dev. 2012;26(3):235-40. Epub 20120119. doi: 10.1101/gad.182618.111. PubMed PMID: 22267412; PubMed Central PMCID: PMCPMC3278890.
39. Pinkert CA. Transgenic Animal Technology: A Laboratory Handbook Elsevier Science; 2002.
40. Miura H, Quadros RM, Gurumurthy CB, Ohtsuka M. Easi-CRISPR for creating knock-in and conditional knockout mouse models using long ssDNA donors. Nat Protoc. 2018;13(1):195-215. Epub 20171221. doi: 10.1038/nprot.2017.153. PubMed PMID: 29266098; PubMed Central PMCID: PMCPMC6058056.

41. Fehr AR, Athmer J, Channappanavar R, Phillips JM, Meyerholz DK, Perlman S. The nsp3 macrodomain promotes virulence in mice with coronavirus-induced encephalitis. J Virol. 2015;89(3):1523-36. Epub 20141126. doi: 10.1128/JVI.02596-14. PubMed PMID: 25428866; PubMed Central PMCID: PMCPMC4300739.
42. Voth LS, O'Connor JJ, Kerr CM, Doerger E, Schwarting N, Sperstad P, et al. Unique Mutations in the Murine Hepatitis Virus Macrodomain Differentially Attenuate Virus Replication, Indicating Multiple Roles for the Macrodomain in Coronavirus Replication. J Virol. 2021;95(15):e0076621. Epub 2021/05/21. doi: 10.1128/JVI.00766-21. PubMed PMID: 34011547; PubMed Central PMCID: PMCPMC8274620.
43. Schaffer PA, Aron GM, Biswal N, Benyesh-Melnick M. Temperature-sensitive mutants of herpes simplex virus type 1: isolation, complementation and partial characterization. Virology. 1973;52(1):57-71. doi: 10.1016/0042-6822(73)90398-x. PubMed PMID: 4372782.
44. Ly CY, Pfannenstiel J, Pant A, Yang Z, Fehr AR, Rodzkin MS, et al. Inhibitors of One or More Cellular Aurora Kinases Impair the Replication of Herpes Simplex Virus 1 and Other DNA and RNA Viruses with Diverse Genomes and Life Cycles. Microbiol Spectr. 2023;11(1):e0194322. Epub 20221220. doi: 10.1128/spectrum.01943-22. PubMed PMID: 36537798; PubMed Central PMCID: PMCPMC9927324.
45. Das SC, Nayak D, Zhou Y, Pattnaik AK. Visualization of intracellular transport of vesicular stomatitis virus nucleocapsids in living cells. J Virol. 2006;80(13):6368-77. doi: 10.1128/JVI.00211-06. PubMed PMID: 16775325; PubMed Central PMCID: PMCPMC1488946.
46. Rodriguez KM, Buch-Larsen SC, Kirby IT, Siordia IR, Hutin D, Rasmussen M, et al. Chemical genetics and proteome-wide site mapping reveal cysteine MARylation by PARP-7 on immune-relevant protein targets. eLife. 2021;10:e60480. doi: 10.7554/eLife.60480.
47. Choi JH, Burke JM, Szymanik KH, Nepal U, Battenhouse A, Lau JT, et al. DUSP11-mediated control of 5'-triphosphate RNA regulates RIG-I sensitivity. Genes Dev. 2020;34(23-24):1697-712. Epub 2020/11/14. doi: 10.1101/gad.340604.120. PubMed PMID: 33184222; PubMed Central PMCID: PMCPMC7706711.

827 **FIGURE LEGENDS**

828 **Fig. 1. PARP14 promotes IFN production following poly(I:C) treatment in human A549**
829 **cells.** A-B) WT (red bars) and PARP14 knock-out (KO) (green bars) A549 cells were
830 transfected with 0.5ug/mL poly(I:C), RNA was isolated from cells at 18 hours post-tranfection
831 (hpt) and IFNβ (A) and IFNλ (B) mRNA levels were quantified by qPCR using ΔCt method.
832 C-D) WT and PARP14 KO cells were transfected with 0.5μg/mL poly(I:C). Supernatant was
833 collected 18 hpt and IFNβ (C) and IFNλ (D) protein levels were quantified by ELISA. Data
834 shown in A-D are from 1 experiment and are representative of 3 independent experiments with
835 N=3 biological replicates for each experiment. E) WT and PARP14 KO cells were either mock
836 transfected or transfected with 0.5 μg/mL of poly(I:C). Cell lysates were collected at 18 hpt
837 and OAS3 and PARP14 protein levels were determined by immunoblotting using β-actin as a
838 loading control. F) Band intensities from E were quantified by densitometry, normalized to β-
839 actin, and then relative levels as compared to mock transfected WT cells were determined.
840 Data shown in E-F are from 1 experiment and are representative of 3 independent experiments
841 with N=1 biological replicate per group in each experiment. G) WT cells were either mock
842 transfected or transfected with 0.5 μg/mL of poly(I:C) and were immediately either treated
843 with DMSO (vehicle) or with increasing concentrations of PARP14i (0.01, 0.1, and 1 μM). At
844 18 hpt RNA was isolated from cells and IFNβ mRNA was quantified by qPCR using ΔCt
845 method. H) WT A549 cells transfected with poly(I:C) were treated with 1 μM PARP14 Degron
846 control (CTL) or PARP14 Degron (DEG) for 18 hours. RNA was isolated from cells at 18 hpt
847 and IFNβ mRNA was quantified by qPCR using ΔCt method. I) WT and PARP14 KO cells
848 were transfected with 0.5 μg of YFP or YFP-PARP14 plasmids. At 48 hpt cells were
849 transfected with 0.5 μg/mL of poly(I:C) and 18 hours later RNA was isolated from cells and
850 IFNβ mRNA was quantified by qPCR using ΔCt method. Data shown in G-I are from 1

851 experiment and are representative of 2-3 independent experiments with N=3 biological
852 replicates per group for each experiment.

853 **Fig. 2. PARP14 promotes IFN production following Mac1 mutant CoV infection.** A)
854 Schematic diagram showing the generation of PARP14 KO mice for Bone-marrow cell
855 isolation. *Parp14* floxed mice were crossed with *cre* heterozygote mice and the resulting
856 progeny were used to harvest bone marrow. Bone marrow cells were isolated and plated with
857 10ng/mL of mCSF or GM-CSF for 6 days to differentiate cells into M0 macrophages or
858 dendritic cells (DCs), respectively. On day 6, these cells were treated with 1μg/mL of 4-
859 hydroxy tamoxifen (4-OHT) for 24 hours to induce *Cre* expression leading to the removal of
860 exon 2 of *Parp14* (for details see Methods). B-C) *Parp14*+/+ (Cre-) (red bars) and *Parp14*-/-
861 (Cre+) (green bars) M0 cells (B) or DCs (C) were infected with MHV WT (solid bars) and
862 N1347A (checkered bars) at an MOI of 0.1. RNA was isolated from cells at 12 hpi and IFNβ
863 mRNA was quantified by qPCR using ΔCt method. D) *Parp14*+/+ cells were infected with
864 WT and N1347A at an MOI of 0.1 and then treated at 1 hpi with DMSO or increasing
865 concentrations of PARP14 inhibitor (PARP14i) (3, 11, 33, 99 and 297nM). RNA was isolated
866 from cells at 12 hpi and IFNβ mRNA levels were quantified using qPCR using ΔCt method.
867 E) *Parp14*+/+ and *Parp14*-/- M0 macrophages were infected with WT and N1347A MHV at
868 an MOI of 0.1 and then treated with DMSO or 100 nM PARP14i at 1 hpi. The cell supernatant
869 was collected at 12 hpi and IFNβ protein was quantified by ELISA. F) A549-ACE2 cells were
870 infected with WT and ΔMac1 SARS-COV-2 at an MOI of 0.1 and treated with DMSO or
871 PARP14i. RNA was isolated from cells at 48 hpi and IFNβ, IFNλ and CXCL10 mRNA levels
872 were quantified by qPCR using ΔCt method. Data shown in B-F are from 1 experiment and

873 are representative of 3 independent experiments with N=3 biological replicates per group for
874 each experiment.

875 **Fig. 3. PARP14 promotes MDA-5 dependent IFN-*β* production.** A) Bone-marrow derived
876 cells were harvested from WT, MAVS$^{-/-}$, MDA-5$^{-/-}$, and RIG-I$^{-/-}$ mice and differentiated into
877 M0 macrophages. Then they were infected with MHV WT or N1347A at an MOI of 0.1. RNA
878 was isolated from cells at 12 hpi and IFNβ mRNA was quantified by qPCR using ΔCt method.
879 The results in A are from one experiment representative of two independent experiments each
880 with N=3 biological replicates per group in each experiment. B) A549 cells were transfected
881 with 0.5 μg/ml of indicated plasmid. Then either DMSO or 100 nM PARP14i were added to
882 the cells 4 hours post-transfection (hpt). RNA was isolated from cells at 24 hpt and IFNβ
883 mRNA was quantified by qPCR using ΔCt method. C-D) BMDMs (C) or A549 cells (D) were
884 infected with either SeV at an MOI of 1 or EMCV at an MOI of 2. 100 nM PARP14i or DMSO
885 was then added 1 hpi. RNA was isolated from cells at 24 hpi (A549 cells) or 36 hpi (BMDMs)
886 and IFNβ mRNA was quantified by qPCR using ΔCt method. The results in B-D are from one
887 experiment representative of three independent experiments each with N=3 biological
888 replicates per group for each experiment.

889 **Fig. 4. PARP14 regulates the transcription of dozens of genes with multiple biological**
890 **functions following MHV-N1347A infection of BMDMs.** A) WT BMDMs were infected
891 with N1347A MHV at an MOI of 0.1 and then treated with DMSO or 100 nM PARP14i at 1
892 hpi. RNA was collected from these cells at 12 hpi and RNAseq was performed to quantify the
893 transcriptome with and without PARP14i. The ratio of gene expression in the presence or
894 absence of PARP14i treatment was plotted against minus $\log_{10}$ value of the p-adjusted value
895 as a volcano plot. B) Gene ontology analysis/pathway enrichment analysis of genes that were

896 identified to be promoted by PARP14 catalytic activity carried out using DAVID gene
897 ontology tool. Pathways enriched with a p-value of less that 0.05 were plotted. C) WT BMDMs
898 were infected with MHV N1347A at an MOI of 0.1 and treated with DMSO or 100 nM
899 PARP14i at 1 hpi. RNA was isolated from cells at 12 hpi and CASP1, FOXO3 and RNF111
900 mRNAs were quantified by qPCR using ΔCt method. RNAseq data shown in A-B are from 1
901 experiment with N=3. Data shown in C are from 1 experiment and are representative of 2
902 independent experiments with N=3 biological replicates per group for each experiment.

903 **Fig. 5. PARP14 inhibits the replication of Mac1-mutant MHV and SARS-CoV-2.** A)
904 *Parp14* floxed *cre+/-* BMDMs were treated with and without 4-OHT. 24 hours later these
905 cells were infected with WT and N1347A MHV at an MOI of 0.1. At 20 hpi cells and
906 supernatants were collected and progeny virus was quantified by plaque assay. B-C) PARP14
907 floxed *cre+* BMDMs (B) and DCs (C) were treated with or without 4-OHT. 24 hours later
908 these cells were infected with WT and N1347A MHV at an MOI of 0.1. At 20 hpi cells and
909 supernatants were collected and progeny virus was quantified by plaque assay. Data shown in
910 A-C are from 1 experiment and are representative of 3 independent experiments with N=3
911 biological replicates per group for each experiment. D) PARP14$^{+/+}$ BMDMs and DCs were
912 infected with WT and N1347A MHV at an MOI of 0.1 and then treated with DMSO or
913 PARP14i (1 μM). At 20hpi cells and supernatants were collected and progeny virus was
914 quantified by plaque assay. Data shown in D are from 1 experiment and are representative of
915 3 independent experiments with N=4 biological replicates per group for each experiment. E)
916 WT Calu-3 cells were either mock-treated or IFNγ-treated (50 Units) O/N. These cells were
917 then infected with WT and ΔMac1 SARS-COV-2 at an MOI of 0.1 and treated with DMSO
918 or PARP14i (1 μM) at 1 hpi. At 48 hpi cells and supernatants were collected and progeny

919 virus was quantified by plaque assay. Data shown in E are from 1 experiment and are
920 representative of 3 independent experiments with N=3 biological replicates per group for
921 each experiment.

922 **Fig. 6. PARP14 restricts the replication of HSV-1 in A549 cells.** A) WT and PARP14 KO
923 A549 cells were infected with HSV-1 at an MOI of 0.01 PFU/cell. Cells and supernatants were
924 collected at indicated time points and progeny virus was quantified by plaque assay. B) WT
925 and PARP14 KO A549 cells were infected with HSV-1 at an MOI of 0.1. At 24 hpi RNA was
926 harvested from infected cells and HSV-1 immediate early gene ICP4, ICP0 and ICP27 mRNAs
927 were quantified by qPCR using ΔCt method having 18S rRNA abundance as the endogenous
928 control. The data in A-B is from 1 experiment representative of 2 independent experiments.
929 N=3 biological replicates per group for each experiment. C) WT A549 cells were infected with
930 HSV-1 at an MOI of 0.01 PFU/cell. At 1 hpi cells were treated with 1 μM PARP14 Degron
931 control (CTL) or PARP14 Degron (DEG). At 24 hpi RNA was harvested from infected cells
932 and HSV-1 immediate early gene ICP4, ICP0 and ICP27 mRNAs were quantified by qPCR
933 using ΔCt method having 18S rRNA abundance as the endogenous control. The data is from 1
934 experiment representative of 2 independent experiments. N=3 biological replicates per group.
935 D) WT and PARP14 KO A549 cells were infected with serial dilutions of HSV-1 starting at a
936 concentration of 1.85×10^9 PFU/ml and plaquing efficiency was determined at 24 hpi. The data
937 in E the combined results of 3 separate experiments, N=9 biological replicates per group. E)
938 WT A549 cells were infected with HSV-1 at an MOI of 0.1 PFU/cell and then treated with
939 DMSO or PARP14i (1 μM) at 1 hpi. Cells and supernatants were collected at 24 hpi and
940 progeny virus was quantified by plaque assay. The data in E is from 1 experiment

941 representative of 2 independent experiments. N=3 biological replicates per group for each
942 experiment.

943 **Fig. 7. PARP14 is required for efficient replication of VSV-GFP in cell culture.** A) A549
944 WT and PARP14 KO cells were infected with VSV-GFP at 1 MOI. At 10 hpi, cells and
945 supernatants were collected and progeny virus was quantified by $TCID_{50}$. Results in A are the
946 combined results of 4 independent experiments. N=12 biological replicates. B) A549-ACE2
947 WT and PARP14 KO cells were infected with VSV-GFP at 1 MOI and then treated with 1 μM
948 PARP14 Degron control (CTL) or PARP14 Degron (DEG) at 1 hpi. At 10 hpi, cells and
949 supernatants were collected and progeny virus was quantified by $TCID_{50}$. Results in B are from
950 one experiment representative of 2 independent experiments. N=3 biological replicates per
951 group for each experiment. C) A549 WT cells were infected with VSV at an MOI of 1 and
952 then treated with DMSO or 100 nM PARP14i (P14i) at 1 hpi. At 10 hpi, cells and supernatants
953 were collected and progeny virus was quantified by $TCID_{50}$. Results in C are the combined
954 results of 4 independent experiments. N=12 biological replicates.

955

956 **SUPPLEMENTAL FIGURE LEGENDS**

957 **Fig. S1.** A) WT and PARP14KO clone 23 (C23) A549 cells were transfected with 0.5μg/mL
958 poly(I:C), at 18 hpt RNA was isolated from cells and the level of IFNβ mRNA was quantified
959 using qPCR using ΔCt method. Data shown in D are from 1 experiment and are representative
960 of 3 independent experiments with N=3 for each experiment. B) WT and PARP14 KO NHDF
961 cells were transfected with 0.5μg/mL poly(I:C), at 18 hpt RNA was isolated from cells and the
962 level of IFNβ mRNA was quantified using qPCR using ΔCt method. Data shown in A are from
963 1 experiment and are representative of 3 independent experiments with N=3 for each
964 experiment. C) 293T cells were mock transfected (M) or transfected with plasmid expressing
965 GFP-PARP14 G832E. At 24 hpt, cells were treated with PARPi for 4 hrs. Cells were then
966 collected and analyzed by immunoblot with indicated antibodies. Data shown in B are from 1
967 experiment representative of 2 independent experiments. D) A549 WT cells were treated with
968 either DMSO, negative control (CTL) or PARP14 Degron (DEG) for 6 hrs and then wither
969 mock transfected or transfected with 0.5μg/mL of poly(I:C) with the corresponding treatments.
970 At 18 hpt cell lysates were collected and PARP14 protein levels were determined by
971 immunoblotting using β-actin as a loading control. E) WT A549 cells transfected with
972 poly(I:C) were treated with 1 μM PARP14 Degron control (CTL) or PARP14 Degron (DEG)
973 for 18 hours. RNA was isolated from cells at 18 hpt and IFNβ mRNA was quantified by qPCR
974 using ΔCt method. Data shown in E are from 1 experiment and are representative of 3
975 independent experiments with N=3 for each experiment.

976 **Fig. S2.** A) Floxed Parp14 *cre*- (*Parp14*+/+) and *cre*+ (*Parp14*-/-) BMDMs were treated with
977 4-OHT and 24 hours later were infected with MHV WT and N1347A at an MOI of 0.1. At
978 12hpi, cell lysates were harvested and levels of PARP14 and β-actin were determined by

979 immunoblotting. B) *Parp14+/+* and *Parp14-/-* BMDMs were infected with WT and N1347A
980 MHV-JHM at an MOI of 0.1. RNA was collected 12 hpi and ISG15 mRNA levels were
981 quantified using qPCR using ΔCt method. Data shown in B are from 1 experiment and are
982 representative of 3 independent experiments with N=3 biological replicates for each
983 experiment. C) RNA was isolated from BMDMs and DCs and CXCR1 mRNA levels were
984 quantified using qPCR using ΔCt method. Data shown in C are the combined data from 2
985 independent experiments with N=6 biological replicates for each group.

986 **Fig. S3. PARP14 does not impact LCMV infection.** A) Gating strategy used to identify
987 $LCMV^{cl13}$(+) cells by flow cytometry. B) WT and PARP14 KO BMDMs were infected with
988 $LCMV^{cl13}$ at an MOI of 1 and the % of $LCMV^{cl13}$ (+) cells were quantified by flow cytometry.
989 These data are from 1 experiment representative of 3 independent experiments. N=3 per group.

990 **Fig S4. PARP14 knockout (KO) in cell lines using CRISPR/Cas9.** Using CRISPR-Cas9
991 based methods, we developed A549-ACE PARP14 KO cells. Western blot confirmed that
992 PARP14 was absent in multiple clones of A549-ACE2 lung epithelial cells.

993 **Fig S5. Reduced VSV replication in A549 PARP14 KO cells is not due to IFN.** A) A549
994 WT and PARP14 KO cells were infected with VSV-GFP at an MOI of 1 and treated with 1
995 μM JAK inhibitor (JAKi). RNA was isolated from cells at 10 hpi and IFN-β mRNA was
996 quantified by qPCR using ΔCt method. Data shown in A are from 1 experiment and are
997 representative of 2 independent experiments with N=3 biological replicates for each
998 experiment. B) A549 WT and PARP14 KO cells were infected with VSV-GFP at an MOI of
999 1 and treated with 1 μM JAK inhibitor (JAKi). RNA was isolated from cells at 10 hpi and
1000 PARP14 mRNA was quantified by qPCR using ΔCt method. Data shown in B are from 1
1001 experiment and are representative of 2 independent experiments with N=3 biological replicates

1002 for each experiment. C) A549 WT and PARP14 KO cells were infected with VSV-GFP at an
1003 MOI of 1 and treated with 1 μM JAK inhibitor (JAKi). At 10 hpi, cells and supernatants were
1004 collected, and the progeny virus was quantified by $TCID_{50}$. Results in C are from one
1005 experiment representative of three independent experiments with N=3 biological replicates for
1006 each experiment.

1007

1008

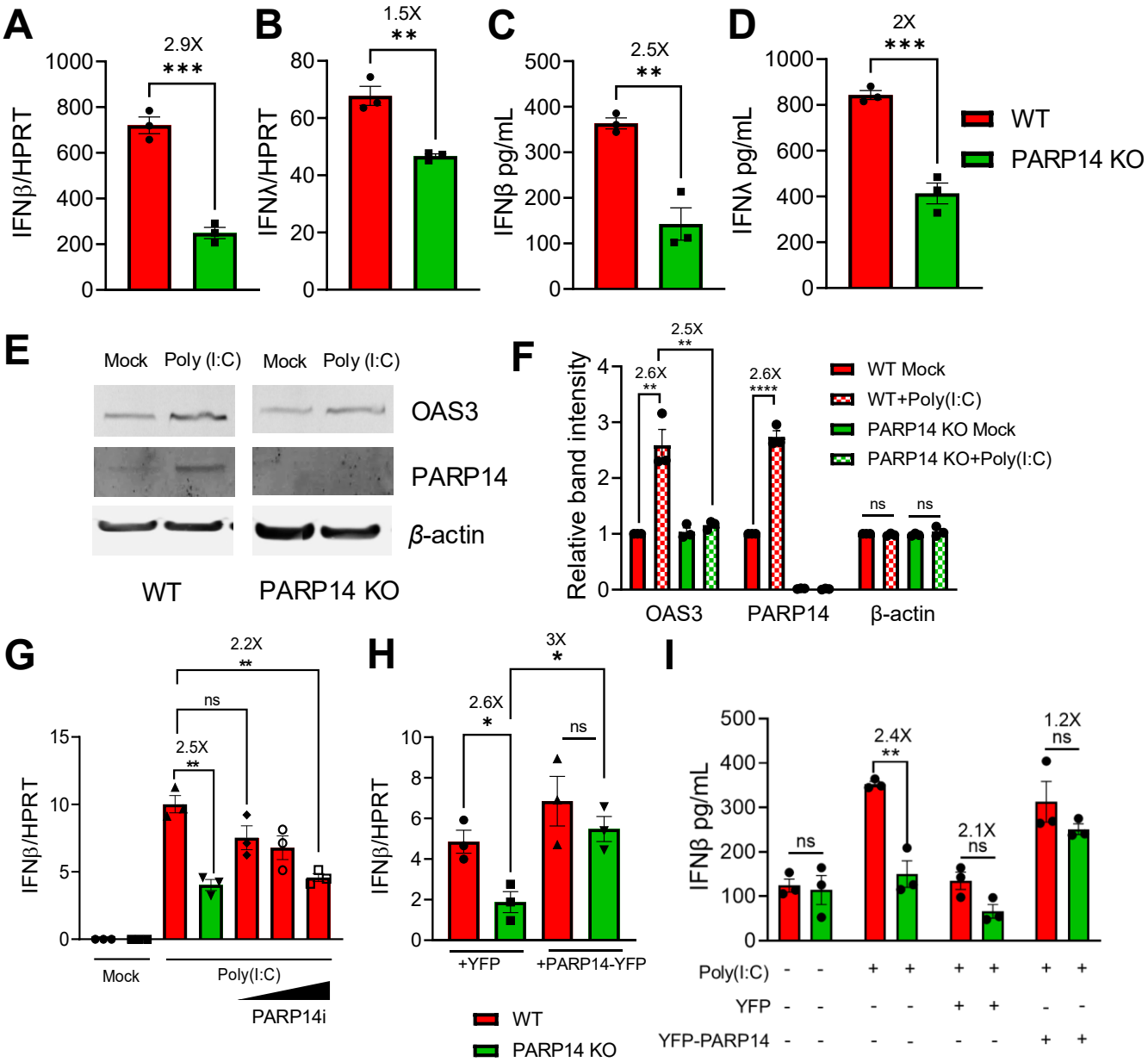
A
2.9X
***
IFNβ/HPRT
1000
800
600
400
200
0
B
1.5X
**
IFNλ/HPRT
80
60
40
20
0
C
2.5X
**
IFNβ pg/mL
500
400
300
200
100
0
D
2X
***
IFNλ pg/mL
1000
800
600
400
200
0
WT
PARP14 KO
E
Mock
Poly (I:C)
Mock
Poly (I:C)
OAS3
PARP14
β-actin
WT
PARP14 KO
F
2.5X
**
2.6X
**
2.6X
****
ns
ns
Relative band intensity
4
3
2
1
0
WT Mock
WT+Poly(I:C)
PARP14 KO Mock
PARP14 KO+Poly(I:C)
OAS3
PARP14
β-actin
G
2.2X
**
ns
2.5X
**
IFNβ/HPRT
15
10
5
0
Mock
Poly(I:C)
PARP14i
H
3X
*
2.6X
*
ns
IFNβ/HPRT
10
8
6
4
2
0
+YFP
+PARP14-YFP
WT
PARP14 KO
I
2.4X
**
1.2X
ns
ns
2.1X
ns
IFNβ pg/mL
500
400
300
200
100
0
Poly(I:C) - - + + + + + +
YFP - - - - + + - -
YFP-PARP14 - - - - - - + +

Fig. 1. PARP14 promotes IFN production following poly(I:C) treatment in human A549 cells. A-B) WT (red bars) and PARP14 knock-out (KO) (green bars) A549 cells were transfected with 0.5ug/mL poly(I:C), RNA was isolated from cells at 18 hours post-tranfection (hpt) and IFNβ (A) and IFNλ (B) mRNA levels were quantified by qPCR using ΔCt method. C-D) WT and PARP14 KO cells were transfected with 0.5μg/mL poly(I:C). Supernatant was collected 18 hpt and IFNβ (C) and IFNλ (D) protein levels were quantified by ELISA. Data shown in A-D are from 1 experiment and are representative of 3 independent experiments with N=3 biological replicates for each experiment. E) WT and PARP14 KO cells were either mock transfected or transfected with 0.5 μg/mL of poly(I:C). Cell lysates were collected at 18 hpt and OAS3 and PARP14 protein levels were determined by immunoblotting using β-actin as a loading control. F) Band intensities from E were quantified by densitometry, normalized to β-actin, and then relative levels as compared to mock transfected WT cells were determined. Data shown in E-F are from 1 experiment and are representative of 3 independent experiments with N=1 biological replicate per group in each experiment. G) WT cells were either mock transfected or transfected with 0.5 μg/mL of poly(I:C) and were immediately either treated with DMSO (vehicle) or with increasing concentrations of PARP14i (0.01, 0.1, and 1 μM). At 18 hpt RNA was isolated from cells and IFNβ mRNA was quantified by qPCR using ΔCt method. H) WT and PARP14 KO cells were transfected with 0.5 μg of YFP or YFP-PARP14 plasmids. At 48 hpt cells were transfected with 0.5 μg/mL of poly(I:C) and 18 hours later RNA was isolated from cells and IFNβ mRNA was quantified by qPCR using ΔCt method. I) WT and PARP14 KO cells were transfected with 0.5 μg of YFP or YFP-PARP14 plasmids. At 48 hpt cells were transfected with 0.5 μg/mL of poly(I:C) and 18 hours later cell supernatant was used to quantify IFNβ protein by ELISA. Data shown in G-I are from 1 experiment and are representative of 2-3 independent experiments with N=3 biological replicates per group for each experiment.

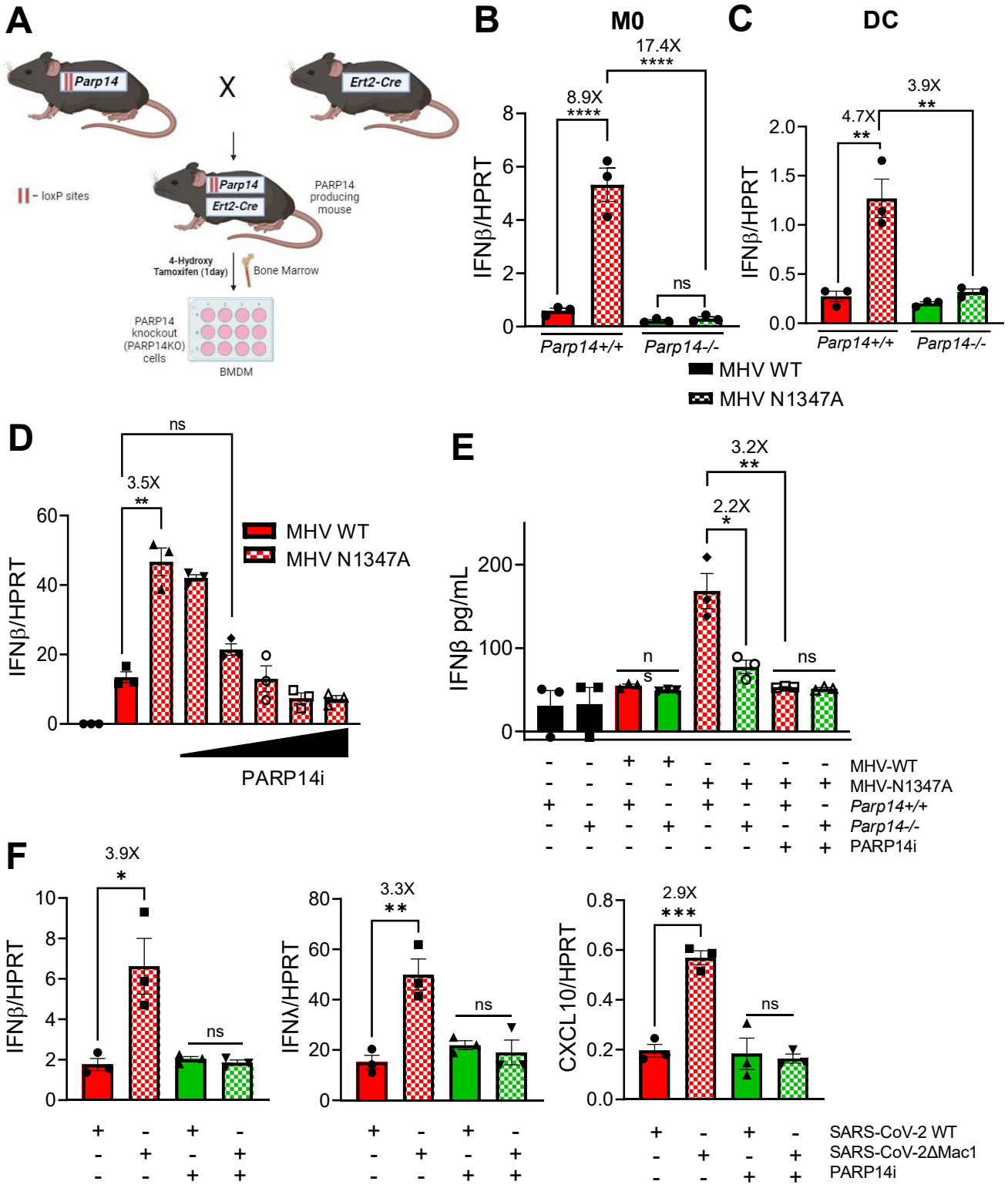
A
Parp14
X
Ert2-Cre
loxP sites
Parp14
Ert2-Cre
PARP14 producing mouse
4-Hydroxy Tamoxifen (1day)
Bone Marrow
PARP14 knockout (PARP14KO) cells
BMDM
B
M0
17.4X
****
8.9X
****
ns
IFNβ/HPRT
Parp14+/+
Parp14-/-
C
DC
3.9X
**
4.7X
**
IFNβ/HPRT
Parp14+/+
Parp14-/-
MHV WT
MHV N1347A
D
ns
3.5X
**
IFNβ/HPRT
MHV WT
MHV N1347A
PARP14i
E
3.2X
**
2.2X
*
IFNβ pg/mL
n
s
ns
MHV-WT
MHV-N1347A
Parp14+/+
Parp14-/-
PARP14i
F
3.9X
*
IFNβ/HPRT
ns
3.3X
**
IFNλ/HPRT
ns
2.9X
***
CXCL10/HPRT
ns
SARS-CoV-2 WT
SARS-CoV-2ΔMac1
PARP14i

Fig. 2. PARP14 promotes IFN production following Mac1 mutant CoV infection. A) Schematic diagram showing the generation of PARP14 KO mice for Bone-marrow cell isolation. *Parp14* floxed mice were crossed with *cre* heterozygote mice and the resulting progeny were used to harvest bone marrow. Bone marrow cells were isolated and plated with 10ng/mL of mCSF or GM-CSF for 6 days to differentiate cells into M0 macrophages or dendritic cells (DCs), respectively. On day 6, these cells were treated with 1µg/mL of 4-hydroxy tamoxifen (4-OHT) for 24 hours to induce *Cre* expression leading to the removal of exon 2 of *Parp14* (for details see Methods). B-C) *Parp14+/+* (Cre-) (red bars) and *Parp14-/-* (Cre+) (green bars) M0 cells (B) or DCs (C) were infected with MHV WT (solid bars) and N1347A (checkered bars) at an MOI of 0.1. RNA was isolated from cells at 12 hpi and IFNβ mRNA was quantified by qPCR using ΔCt method. D) *Parp14+/+* cells were infected with WT and N1347A at an MOI of 0.1 and then treated at 1 hpi with DMSO or increasing concentrations of PARP14 inhibitor (PARP14i) (3, 11, 33, 99 and 297nM). RNA was isolated from cells at 12 hpi and IFNβ mRNA levels were quantified using qPCR using ΔCt method. E) *Parp14+/+* (red) and *Parp14-/-* (green) M0 macrophages were infected with WT (solid bars) and N1347A (checkered bars) MHV at an MOI of 0.1 and then treated with DMSO or 100 nM PARP14i at 1 hpi. The cell supernatant was collected at 12 hpi and IFNβ protein was quantified by ELISA. F) A549-ACE2 cells were infected with WT (solid bars) and ∆Mac1 (checkered bars) SARS-COV-2 at an MOI of 0.1 and treated with DMSO (red) or PARP14i (green). RNA was isolated from cells at 48 hpi and IFNβ, IFNλ and CXCL10 mRNA levels were quantified by qPCR using ΔCt method. Data shown in B-F are from 1 experiment and are representative of 3 independent experiments with N=3 biological replicates per group for each experiment.

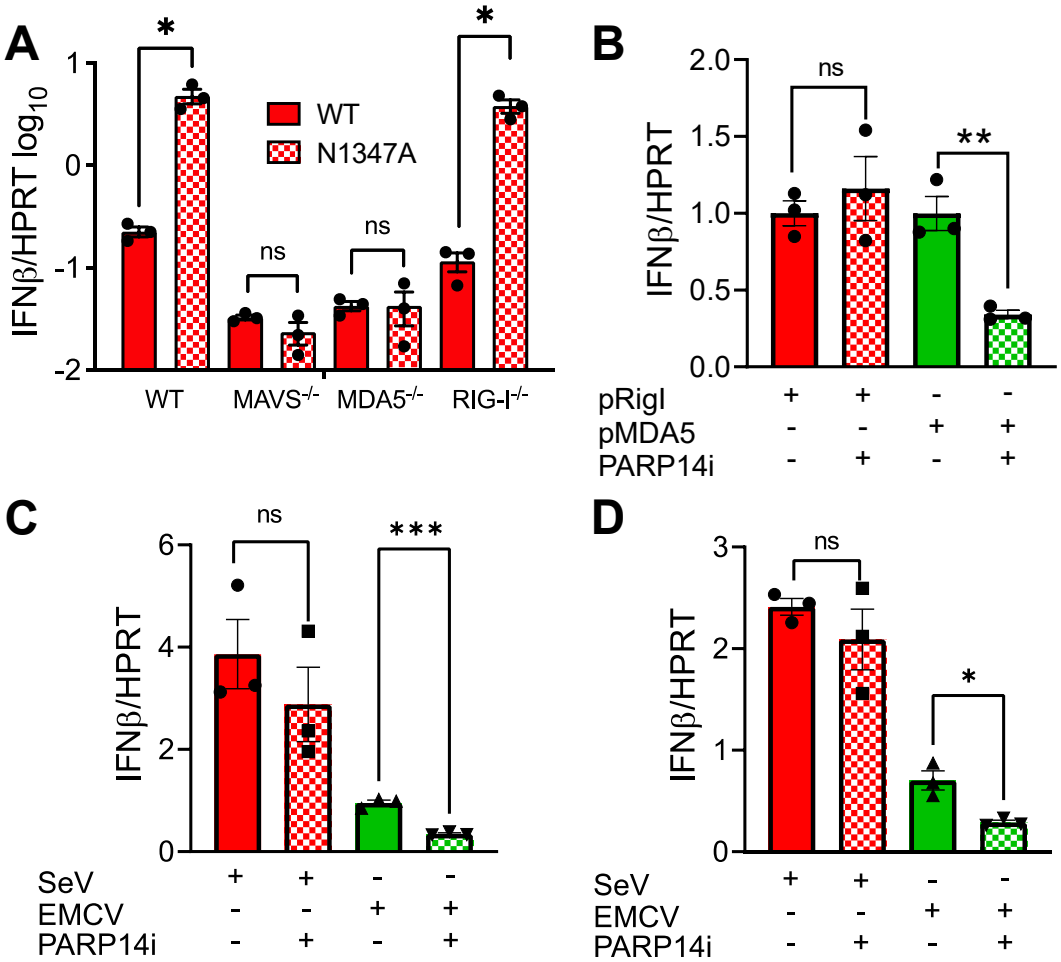

Fig. 3. PARP14 promotes MDA-5 dependent IFN-β production. A) Bone-marrow derived cells were harvested from WT, MAVS$^{-/-}$, MDA-5$^{-/-}$, and RIG-I$^{-/-}$ mice and differentiated into M0 macrophages. Then they were infected with MHV WT or N1347A at an MOI of 0.1. RNA was isolated from cells at 12 hpi and IFNβ mRNA was quantified by qPCR using ΔCt method. The results in A are from one experiment representative of two independent experiments each with N=3 biological replicates per group in each experiment. B) A549 cells were transfected with 0.5 μg/ml of indicated plasmid. Then either DMSO or 100 nM PARP14i were added to the cells 4 hours post-transfection (hpt). RNA was isolated from cells at 24 hpt and IFNβ mRNA was quantified by qPCR using ΔCt method. C-D) BMDMs (C) or A549 cells (D) were infected with either SeV at an MOI of 1 or EMCV at an MOI of 2. 100 nM PARP14i or DMSO was then added 1 hpi. RNA was isolated from cells at 24 hpi (A549 cells) or 36 hpi (BMDMs) and IFNβ mRNA was quantified by qPCR using ΔCt method. The results in B-D are from one experiment representative of three independent experiments each with N=3 biological replicates per group for each experiment.

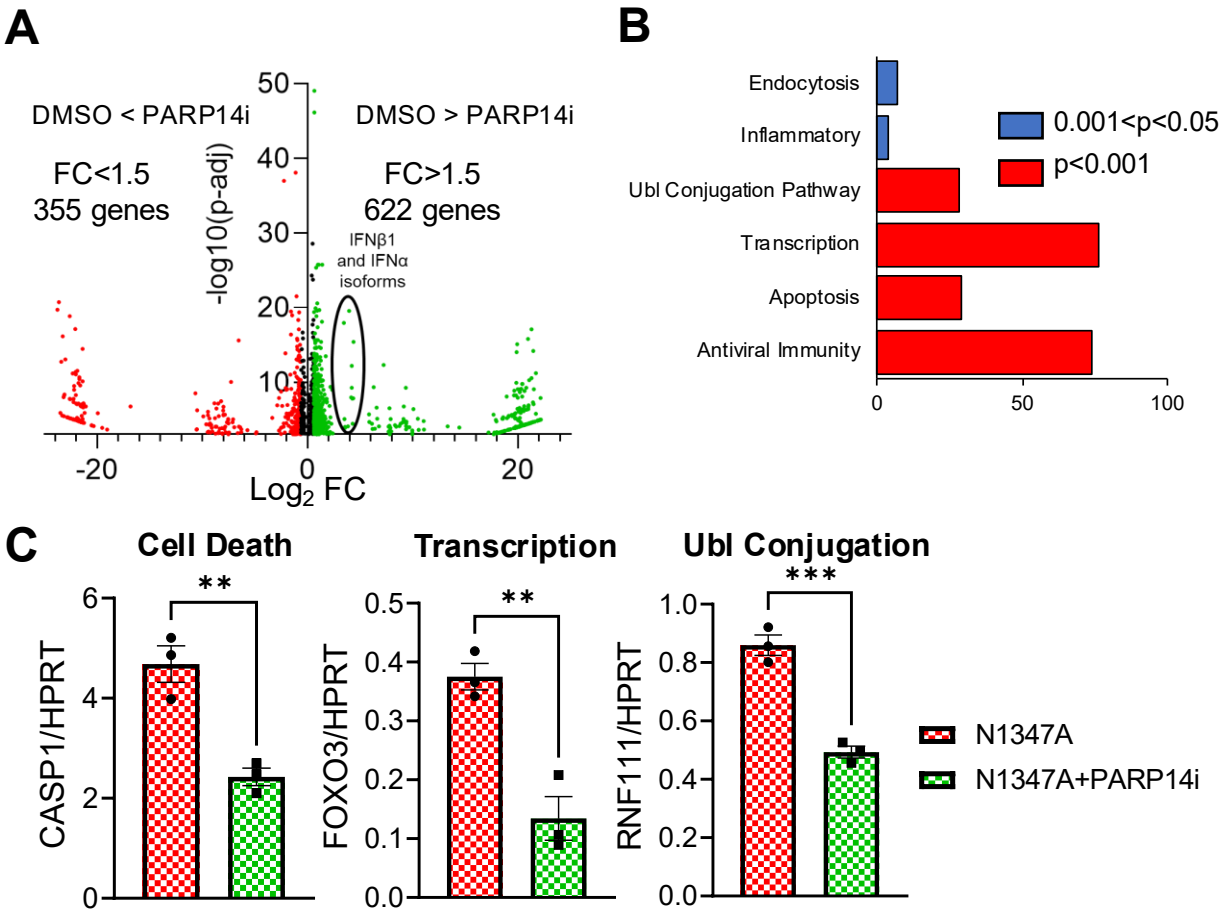

Fig. 4. PARP14 regulates the transcription of dozens of genes with multiple biological functions following MHV-N1347A infection of BMDMs. A) WT BMDMs were infected with N1347A MHV at an MOI of 0.1 and then treated with DMSO or 100 nM PARP14i at 1 hpi. RNA was collected from these cells at 12 hpi and RNAseq was performed to quantify the transcriptome with and without PARP14i. The ratio of gene expression in the presence or absence of PARP14i treatment was plotted against minus $\log_{10}$ value of the p-adjusted value as a volcano plot. B) Gene ontology analysis/pathway enrichment analysis of genes that were identified to be promoted by PARP14 catalytic activity carried out using DAVID gene ontology tool. Pathways enriched with a p-value of less that 0.05 were plotted. C) WT BMDMs were infected with MHV N1347A at an MOI of 0.1 and treated with DMSO or 100 nM PARP14i at 1 hpi. RNA was isolated from cells at 12 hpi and CASP1, FOXO3 and RNF111 mRNAs were quantified by qPCR using ΔCt method. RNAseq data shown in A-B are from 1 experiment with N=3. Data shown in C are from 1 experiment and are representative of 2 independent experiments with N=3 biological replicates per group for each experiment.

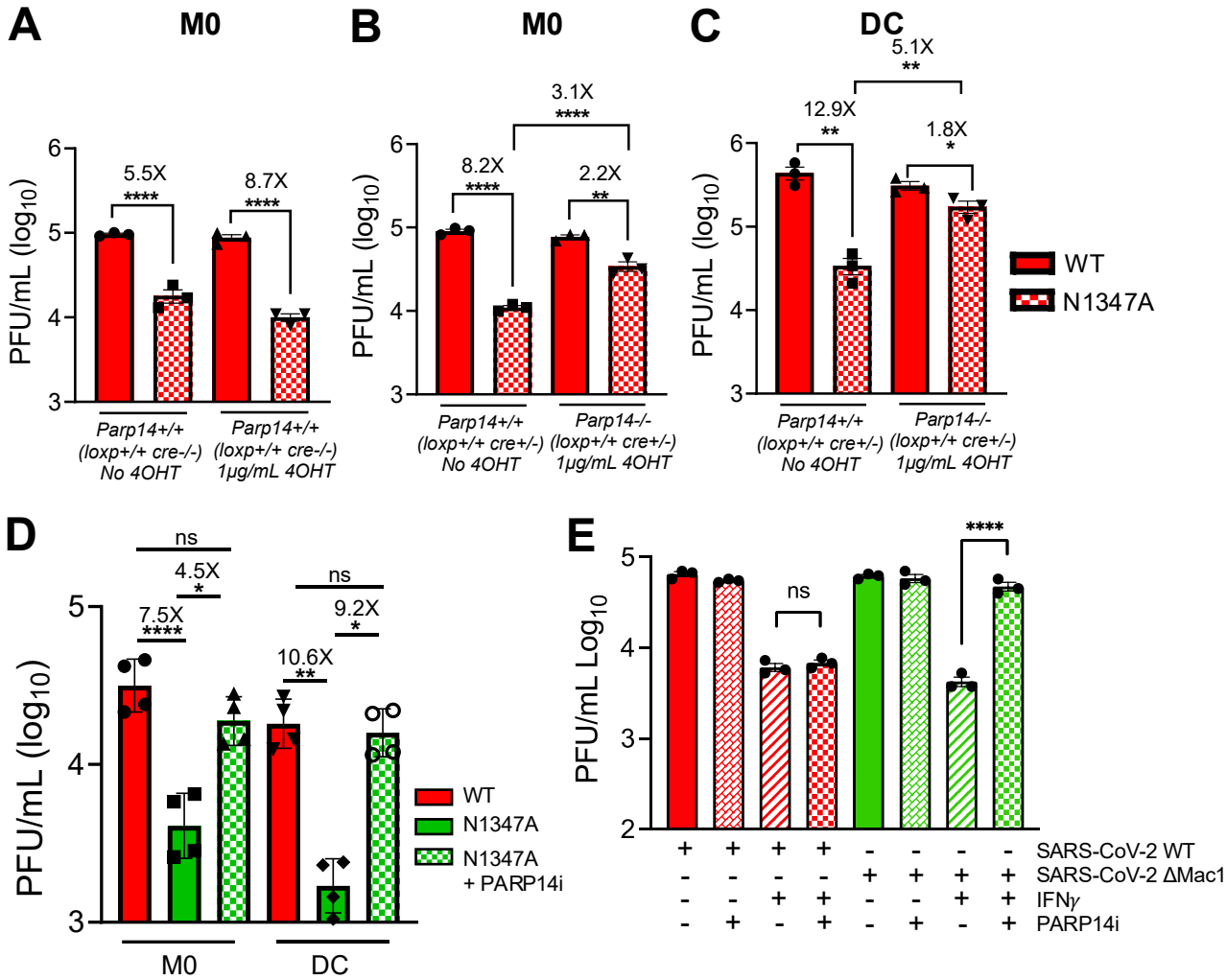

Fig. 5. PARP14 inhibits the replication of Mac1-mutant MHV and SARS-CoV-2. A) *Parp14* floxed *cre+/-* BMDMs were treated with and without 4-OHT. 24 hours later these cells were infected with WT and N1347A MHV at an MOI of 0.1. At 20 hpi cells and supernatants were collected and progeny virus was quantified by plaque assay. B-C) PARP14 floxed *cre+* BMDMs (B) and DCs (C) were treated with or without 4-OHT. 24 hours later these cells were infected with WT and N1347A MHV at an MOI of 0.1. At 20 hpi cells and supernatants were collected and progeny virus was quantified by plaque assay. Data shown in A-C are from 1 experiment and are representative of 3 independent experiments with N=3 biological replicates per group for each experiment. D) PARP14$^{+/+}$ BMDMs and DCs were infected with WT and N1347A MHV at an MOI of 0.1 and then treated with DMSO or PARP14i (1 μM). At 20hpi cells and supernatants were collected and progeny virus was quantified by plaque assay. Data shown in D are from 1 experiment and are representative of 3 independent experiments with N=4 biological replicates per group for each experiment. E) WT Calu-3 cells were either mock-treated or IFNγ-treated (50 Units) (shown with different patterns)O/N. These cells were then infected with WT (red bars) and ΔMac1 (green bars) SARS-COV-2 at an MOI of 0.1 and treated with DMSO or PARP14i (1 μM) (shown with different patterns) at 1 hpi. At 48 hpi cells and supernatants were collected and progeny virus was quantified by plaque assay. Data shown in E are from 1 experiment and are representative of 3 independent experiments with N=3 biological replicates per group for each experiment.

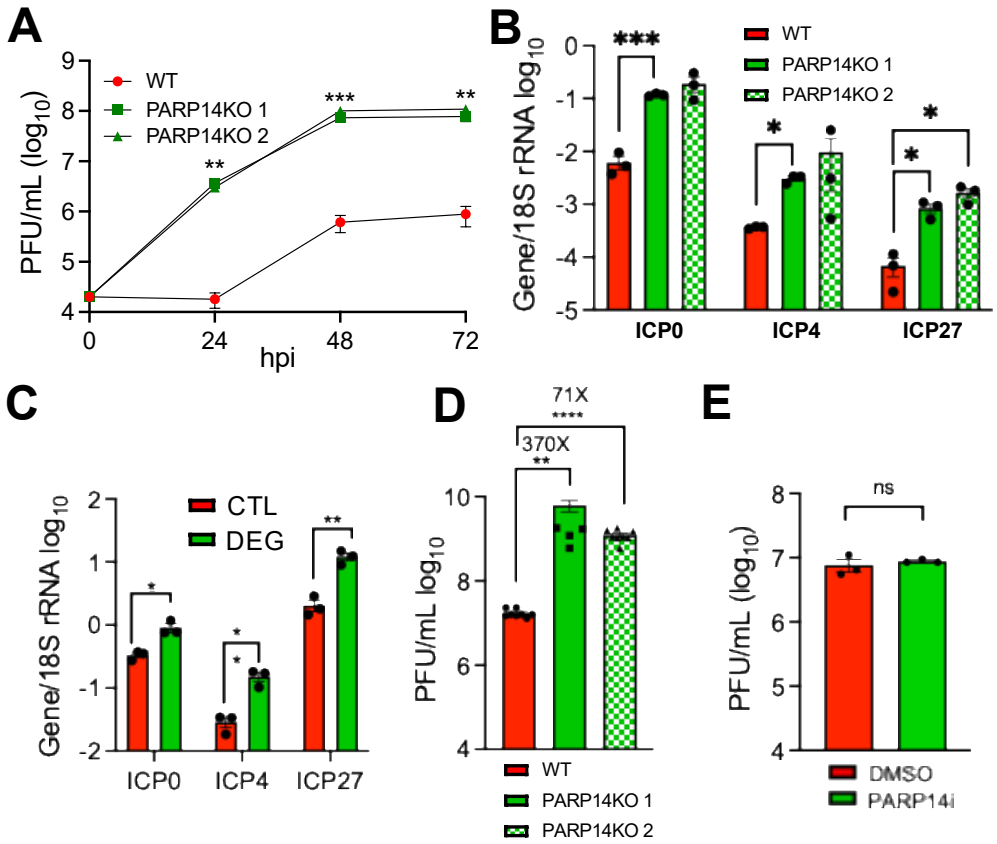

Fig. 6. PARP14 restricts the replication of HSV-1 in A549 cells. A) WT and PARP14 KO A549 cells were infected with HSV-1 at an MOI of 0.01 PFU/cell. Cells and supernatants were collected at indicated time points and progeny virus was quantified by plaque assay. B) WT and PARP14 KO A549 cells were infected with HSV-1 at an MOI of 0.1. At 24 hpi RNA was harvested from infected cells and HSV-1 immediate early gene ICP4, ICP0 and ICP27 mRNAs were quantified by qPCR using ΔCt method having 18S rRNA abundance as the endogenous control. The data in A-B is from 1 experiment representative of 2 independent experiments. All statistical comparison not shown were not significant. N=3 biological replicates per group for each experiment. C) WT A549 cells were infected with HSV-1 at an MOI of 0.01 PFU/cell. At 1 hpi cells were treated with 1 μM PARP14 Degron control (CTL) or PARP14 Degron (DEG). At 24 hpi RNA was harvested from infected cells and HSV-1 immediate early gene ICP4, ICP0 and ICP27 mRNAs were quantified by qPCR using ΔCt method having 18S rRNA abundance as the endogenous control. The data is from 1 experiment representative of 2 independent experiments. N=3 biological replicates per group. D) WT and PARP14 KO A549 cells were infected with serial dilutions of HSV-1 starting at a concentration of 1.85×10^{9} PFU/ml and plaquing efficiency was determined at 24 hpi. The data in D is the combined results of 3 separate experiments, N=9 biological replicates per group. E) WT A549 cells were infected with HSV-1 at an MOI of 0.1 PFU/cell and then treated with DMSO or PARP14i (1 μM) at 1 hpi. Cells and supernatants were collected at 24 hpi and progeny virus was quantified by plaque assay. The data in E is from 1 experiment representative of 2 independent experiments. N=3 biological replicates per group for each experiment.

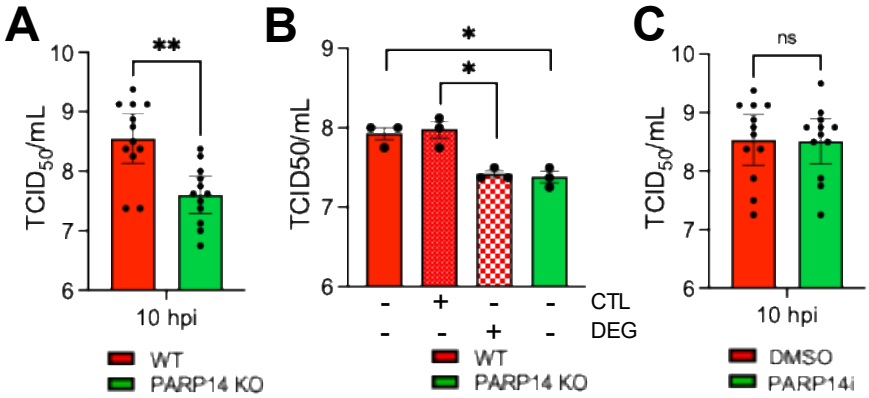

Fig. 7. PARP14 is required for efficient replication of VSV-GFP in cell culture. A) A549 WT and PARP14 KO cells were infected with VSV-GFP at 1 MOI. At 10 hpi, cells and supernatants were collected and progeny virus was quantified by $TCID_{50}$. Results in A are the combined results of 4 independent experiments. N=12 biological replicates. B) A549-ACE2 WT and PARP14 KO cells were infected with VSV-GFP at 1 MOI and then treated with 1 μM PARP14 Degron control (CTL) or PARP14 Degron (DEG) at 1 hpi. At 10 hpi, cells and supernatants were collected and progeny virus was quantified by $TCID_{50}$. Results in B are from one experiment representative of 2 independent experiments. N=3 biological replicates per group for each experiment. C) A549 WT cells were infected with VSV at an MOI of 1 and then treated with DMSO or 100 nM PARP14i (P14i) at 1 hpi. At 10 hpi, cells and supernatants were collected and progeny virus was quantified by $TCID_{50}$. Results in C are the combined results of 4 independent experiments. N=12 biological replicates.